Emergence of blueschists on Earth linked to secular changes in oceanic crust composition

Article *in* Nature Geoscience · January 2016

DOI: 10.1038/ngeo2605

CITATIONS
43

READS
642

2 authors:

Richard Mark Palin
University of Oxford
68 PUBLICATIONS **790** CITATIONS
SEE PROFILE

R. W. White
Johannes Gutenberg-Universität Mainz
99 PUBLICATIONS **6,665** CITATIONS
SEE PROFILE

Richard Palin (richardmpalin@gmail.com)

Emergence of blueschists on Earth linked to secular changes in oceanic crust composition

Richard M. Palin* and Richard W. White

Institute of Geosciences, Johannes-Gutenberg University Mainz, 55128 Mainz, Germany

* corresponding author: richardmpalin@gmail.com

The oldest blueschists – metamorphic rocks formed during subduction – are of Neoproterozoic age[1], and 0.7 to 0.8 billion years old. Yet, subduction of oceanic crust to mantle depths is thought to have occurred since the Hadean, over 4 billion years ago[2]. Blueschists typically form under cold geothermal gradients of less than 400 °C GPa^{-1}, so their absence in the ancient rock record is typically attributed to hotter pre-Neoproterozoic mantle prohibiting such low-temperature metamorphism; however, modern analogues of Archean subduction suggest that blueschist-facies metamorphic conditions are attainable at the slab surface[3]. Here we show that the absence of blueschists in the ancient geological record can be attributed to the changing composition of oceanic crust throughout Earth history, which is a consequence of secular cooling of the mantle since the Archean[4]. Oceanic crust formed on the hot, early Earth would have been rich in magnesium oxide (MgO). We use phase equilibria calculations to show that blueschists do not form in high-MgO rocks under subduction-related geothermal gradients. Instead, the subduction of MgO-rich oceanic crust would have created greenschist-like rocks – metamorphic rocks formed today at low temperatures and pressures. These ancient metamorphic products can hold about 20%

more water than younger metamorphosed oceanic crust, implying that the global hydrological cycle was more efficient in the deep geological past than today.

Blueschists are glaucophane-bearing meta-basalts[5,6] that form at high-pressure–low-temperature (H*P*–L*T*) conditions in the Earth, typically along geothermal gradients of 150–400 °C/GPa. As such conditions only occur today in subduction zones, blueschists are a diagnostic petrological signature of the operation of modern-day subduction-driven plate tectonics, with the cause of their apparent absence from the first ~3.8 Gyr of Earth history being a highly controversial topic. Some workers propose that modern-day plate tectonics initiated during the Neoproterozoic[7,8] (0.5–1.0 Ga) with the absence of subduction prior to this geodynamic transition prohibiting their formation. However, numerous studies suggest that subduction-related processes operated on the early Earth during the Palaeoarchean[9] (3.2–3.6 Ga), the Eoarchean[10] (3.6–4.0 Ga), and even the Hadean[2] (>4.0 Ga). Although a hotter Archean mantle[4] reputedly caused subduction to proceed along elevated geothermal gradients[11], numerical modelling shows that the thermal structure of subduction zones is primarily controlled by the convergence rate and age of subducting lithosphere, with ambient mantle temperature imparting a second-order effect[12,13]. Modern-day convergent margins exhibiting plate-tectonic velocities and subducted-crust ages similar to purported Archean values (see Supplementary Information) exhibit slab-top geotherms in the range ~280–380 °C/GPa at 0.5–2.5 GPa[3]. As such, it is sensible to consider that metamorphism of hydrated oceanic crust under such blueschist-facies H*P*–L*T* conditions occurred during pre-Neoproterozoic times, the consequences of which we investigate herein.

Here, we present a petrological explanation for the apparent absence of blueschists in the early-Earth geological record, which has received no consideration in previous works. Alhough higher mantle temperatures may not have appreciably affected subduction-zone thermal structures, they will have directly controlled the composition of primary crust

generated at mid-ocean ridge (MOR) systems. Mantle potential temperatures have decreased throughout Earth history from ~1500–1600 °C at c. 2.5–3.0 Ga to ~1350 °C today[4]. Consequently, oceanic crust on the early Earth is thought to have been significantly more magnesian than modern MOR basalt[15], which contains ~8 wt% MgO (Table S1). This compositional trend has been confirmed in non-arc basalts from Archean and Proterozoic greenstone terranes[16].

We investigate the petrological effects of secular cooling by forward-modelling the equilibrium (minimum Gibbs free energy) mineral assemblages that would develop during H*P*–L*T* metamorphism of four natural lithologies representative of MOR-derived oceanic crust: a Palaeoarchean high-MgO basalt with ~16.2 wt% MgO, a Palaeoproterozoic olivine-bearing basalt with ~14.1 wt% MgO, a Mesoproterozoic gabbro with ~11.2 wt% MgO, and a pillow basalt from the Neoproterozoic–Palaeozoic boundary with ~9.7 wt% MgO (Table S1). This range in MgO content is similar to that proposed for geochemical models of Archean–Proterozoic oceanic crust (11–15 wt% MgO)[17]. Age and full bulk-rock compositional data are given in Tables S1 and S2. From these calculated mineral assemblages, we identify different metamorphic rock types that characterise potential cold and warm Archean and Proterozoic subduction zones. Varying proportions of hydrous minerals that would stabilise during prograde metamorphism are used to calculate fluid budgets for each descending slab and constrain the *P–T* conditions under which major dehydration reactions occur. From these results, we draw important conclusions about the changing petrological character of subduction-zone metamorphism and the potential efficiency of fluid transfer between the hydrosphere and upper mantle throughout Earth history.

Metamorphic rock types calculated to be stable between 0.5–2.5 GPa and 300–650 °C are shown in Fig. 1, with glaucophane stability indicated by stippled regions. Modebox plots showing the proportions of minerals occurring along a warm geotherm (350 °C/GPa) are

given in Fig. 2. Fully labelled phase diagrams are presented in Fig. S1 and modebox plots showing mineral assemblages along a cold geotherm (250 °C/GPa) are shown in Fig. S2. Additional detail regarding phase equilibria modelling procedures is given in the Methods section and the Supplementary Information.

MgO-rich (Fig. 1a) and olivine-bearing basalts (Fig. 1b) only form glaucophane-bearing assemblages between ~0.8–1.4 GPa and ~390–500 °C. Outside of this *P–T* range, warm-subduction assemblages in both protoliths are dominated by actinolite and chlorite – together comprising ~75% modal proportion – with subsidiary (1–10% each) lawsonite, epidote, zoisite, clinopyroxene, sphene, rutile, quartz, muscovite, biotite, and/or garnet, depending on metamorphic grade (Fig. 2a–b). Here, the proportion of lawsonite would be strongly influenced by the H_2O content of the bulk composition and would be considerably reduced if the rock could not maintain fluid saturation[18]. Assemblages formed during cold subduction, typical of *P–T* conditions recorded by Phanerozoic and Neoproterozoic blueschists[19], are largely similar, though lack epidote and zoisite, and additionally contain talc and tremolite at high-grade conditions (Fig. S2). Notably, deep subduction along either geotherm would form garnet-pyroxenite or garnet-hornblendite (Fig. 1), not eclogite, as diopside would be stable instead of omphacite (Figs 2a–b and S2).

By contrast, sodic amphibole is significantly more stable in MgO-poor (≤11.2 wt%) bulk compositions representative of Mesoproterozoic–Neoproterozoic oceanic crust (Figs 1c–d) and diagnostic blueschist-facies assemblages occur over a wider *P–T* range. Lawsonite-blueschists containing up to ~30% glaucophane would form during cold subduction (Fig. S2), ultimately transforming to eclogite at T >525 °C (Fig. 1c–d). Metamorphism along a warm geotherm would form epidote-blueschist in both cases, containing up to ~40% glaucophane (Fig. 2c–d). Calculated bulk-rock densities for all lithologies along either cold or warm geotherms are remarkably similar (~3.10–3.15 g/cm^3), despite the different mineralogies, and

99 only increase significantly when garnet stabilises (Figs 2 and S2). As these densities do not
100 exceed ~3.30 g/cm^3 proposed for Archean sub-continental lithospheric mantle[20], their
101 exhumation to crustal depths should not be prohibited by a negative-buoyancy contrast;
102 however, the mechanisms of exhumation of high-*P* rocks are poorly understood, even in
103 modern-day tectonic settings[21]. Differences in the petrophysical characteristics of modern and
104 ancient mantle and oceanic lithosphere[22] alongside sluggish plate velocities may have
105 promoted the deep-subduction of oceanic crust, but resisted its exhumation back to the
106 surface[23]. Consequently, the formation, but lack of exhumation, of high-*P* rocks during
107 subduction may additionally have contributed to their scarcity in ancient geological terranes.
108 Nonetheless, even if exhumation readily occurred, the preservation of H*P*–L*T* mineral
109 assemblages is problematic, requiring it to be rapid, largely deformation- and fluid-free, and
110 accompanied by substantial cooling[18]. In particular, despite being stable over a wide range of
111 subduction-related *P*–*T* conditions (Fig. 1), lawsonite is rarely preserved in exhumed rocks,
112 instead decomposing to chlorite, zoisite, paragonite, and/or quartz[24,25]. The petrological
113 products of subducted high-MgO and olivine-bearing ocean crust – if exhumed – may
114 therefore closely resemble those that characterise lower-*P* greenschist-facies metabasites
115 (Figs 1 and S1), illustrating the potential for misidentification of subduction-related mafic–
116 ultramafic components of Archean greenstone belts as having formed in crustal environments.
117 However, discrimination between these tectonic scenarios should be possible on the basis of
118 constituent mineral chemistry, as actinolite compositions calculated along high-*P* geotherms
119 for high-MgO bulk compositions are more sodic and magnesian than those at equivalent
120 temperatures in the greenschist facies (Fig. S3).
121 What consequences does this secular compositional change have for subduction-zone
122 hydrodynamics? The dehydration of subducted crustal material is a major process within the
123 global geological water cycle, directly influencing arc magmatism and the physical properties

of the subducting slab and overlying mantle wedge[13]. Key dehydration reactions that would occur during warm subduction of Archean high-MgO basalt and Neoproterozoic low-MgO basalt are shown in Figs 3a and 3b, respectively, and calculated proportions of hydrous phases have allowed determination of the water budgets for each descending slab (Supplementary Information). Assuming that low-grade mineral assemblages in the shallow portion of the subduction channel (10–15 km) are minimally fluid-saturated, ~20 mol. % of the initially subducted structurally bound H_2O would be released simultaneously in both protoliths via the decomposition of lawsonite at P ~1.1–1.2 GPa, equivalent to a depth of 40–45 km (Fig. S4). Significant further dehydration occurs at ~1.4–1.7 GPa (50–60 km) via the breakdown of chlorite (and minor epidote) to produce garnet, where 40% more H_2O is released over just 50–60 °C (Fig. S4). Fluid loss would continue with increasing metamorphism as amphibole destabilises, with near-complete dehydration (>90% H_2O loss) achieved at ~2.1–2.2 GPa (75–80 km).

It has previously been supposed that the transport of H_2O from the hydrosphere into the Earth's interior was significantly less efficient during the Archean than occurs today due to higher mantle potential temperatures thought to have dehydrated subducted materials at shallower depths[26]. However, numerical modelling refutes the proposition that Archean subduction necessarily occurred along exceptionally hot geotherms[3]. Fully hydrated high-MgO metabasalt has the capacity to hold ~20% more water (5.93 wt%) within constituent hydrous phases than modern-day low-MgO metabasalt can (4.9 wt%) under equivalent P–T conditions (Fig. S4), owing to a larger combined proportion of chlorite and amphibole (Fig. 2). Additionally, a bulk composition that is more magnesian and less aluminous than a Neoproterozoic or modern MOR basalt (Table S2) delays the onset of garnet growth during metamorphism (Fig. 1a–d), allowing chlorite to stably persist to higher temperatures and dehydrate at greater depths in the subduction channel (Fig. 3). The transport of volatiles from

149 the hydrosphere to the Earth's interior was thus likely to have been more efficient during the
150 Archean than today, in contrast to previous studies' assumptions[26]. Although the actual depths
151 of subduction-dehydration are contingent on the dip angle, age, and convergence rate of the
152 subducting slab[27], the majority of fluid loss from the oceanic crust during Neoproterozoic and
153 Archean subduction is predicted to occur at upper-mantle depths (40–80 km).
154 Our results show for the first time that the apparent absence of blueschists from the
155 early-Earth geological record can be accounted for by the changing chemical composition of
156 oceanic crust throughout Earth history: a consequence of secular cooling of the mantle since
157 the Archean[4]. The prior lack of investigation into the petrological evolution of subducted
158 high-MgO basalt has restricted our understanding of early-Earth tectonics. The limited *P–T*
159 range over which sodic amphibole forms (Fig. 1a–b), coupled with the extreme difficulty in
160 preserving lawsonite (if present) during exhumation, mean that the petrological products of
161 subduction-metamorphism in Archean–Paleoproterozoic terranes will be significantly
162 different than those in Mesoproterozoic–Phanerozoic terranes, even if formed at equivalent
163 H*P*–L*T* conditions. Such differences may also account for the paucity of eclogite in the early-
164 Earth geological record, with omphacite-absent garnet–clinopyroxenite shown to be stable at
165 high-*P* conditions instead (Fig. 2a–b). Consequently, the application of modern-day
166 classification systems[5,6] to identification of ancient subduction-zone metamorphism is
167 untenable in a natural system that is strongly asymmetric, as they are dependent upon low-
168 MgO modern MOR basalt compositions. Feldspar-absent, Na-rich actinolite- and chlorite-
169 dominated rocks that may have previously been interpreted as having formed at lower-*P*
170 greenschist-facies crustal conditions offer important opportunity for re-examination in the
171 search for petrological evidence of ancient subduction.
172
173 **References**

1. Maruyama, S., Liou, J.G., & Terabayashi, M. Blueschists and eclogites of the world and their exhumation. *Int. Geol. Rev.* **38**, 485–594 (1996).
2. Turner, S., Rushmer, T., Reagan, M., & Moyen, J.F. Heading down early on? Start of subduction on Earth. *Geology* **42**, 139–142 (2014).
3. Syracuse, E.M., van Keken, P.E. & Abers, G.A. The global range of subduction zone thermal models. *Phys. Earth Planet. In.* **183**, 73–90 (2010).
4. Herzberg, C., Condie, K. & Korenaga, J. Thermal history of the Earth and its petrological expression. *Earth Planet. Sci. Lett.* **292**, 79–88 (2010).
5. Bailey, E.H. Metamorphic facies of the Franciscan formation of California and their geologic significance. *Geol. S. Am. S.* **68**, 4–5 (1961).
6. Ernst, W.G. Petrogenesis of glaucophane schists. *J. Petrol.* **4**, 1–30 (1963).
7. Stern, R.J. Evidence from ophiolites, blueschists, and ultrahigh-pressure metamorphic terranes that the modern episode of subduction tectonics began in Neoproterozoic time. *Geology* **33**, 557–560 (2005).
8. Hamilton, W.B. Plate tectonics began in Neoproterozoic time, and plumes from the deep mantle have never operated. *Lithos* **123**, 1–20 (2011).
9. Shirey, S.B. & Richardson, S.H. Start of the Wilson Cycle at 3 Ga shown by diamonds from subcontinental mantle. *Science* **333**, 434–436 (2011).
10. Furnes, H., de Wit, M., Staudigel, H., Rosing, M. & Muehlenbachs, K. A vestige of Earth's oldest ophiolite. *Science* **315**, 1704–1707 (2007).
11. Martin, H. & Moyen, J.F. Secular changes in tonalite–trondhjemite–granodiorite composition as markers of the progressive cooling of Earth. *Geology* **30**, 319–322 (2002).
12. Kirby, S.H., Durham, W.B. & Stern, L.A. Mantle phase changes and deep-earthquake faulting in subducting lithosphere. *Science* **252**, 216–225 (1991).

13. Peacock, S.M. Thermal and petrologic structure of subduction zones. In Bebout, G.E., et al., eds., *Subduction: Top to Bottom*. Geophysical Monograph of the American Geophysical Union **96**, 119–133 (1996).
14. Hargraves, R.B. Faster spreading or greater ridge length in the Archean? *Geology* **14**, 750–752 (1986).
15. Foley, S.F., Buhre, S. & Jacob, D.E. Evolution of the Archean crust by delamination and shallow subduction. *Nature* **421**, 249–252 (2003).
16. Furnes, H., Dilek, Y. & de Wit, M. Precambrian greenstone sequences represent different ophiolite types. *Gondwana Res.* **27**, 649–685 (2014).
17. Ziaja, K., Foley, S.F., White, R.W. & Buhre, S. Metamorphism and melting of picritic crust in the early Earth. *Lithos* **189**, 173–184 (2014).
18. Clarke, G.L., Powell, R. & Fitzherbert, J.A. The lawsonite paradox: a comparison of field evidence and mineral equilibria modelling. *J. Met. Geol.* **24**, 715–725 (2006).
19. Brown, M. Duality of thermal regimes is the distinctive characteristic of plate tectonics since the Neoarchean. *Geology* **34**, 961–964 (2006).
20. Griffin, W.L., et al. The origin and evolution of Archean lithospheric mantle. *Precambrian Res.* **127**, 19–41 (2003).
21. Warren, C.J., Beaumont, C. & Jamieson, R.A. Modelling tectonic styles and ultra-high pressure (UHP) rock exhumation during the transition from oceanic subduction to continental collision. *Earth Planet. Sci. Lett.* **267**, 129–45 (2008).
22. Korenaga, J. Initiation and evolution of plate tectonics on Earth: Theories and observations. *Annu. Rev. Earth Sci.* **41**, 117–51 (2013).
23. Husson, L., Brun, J.P., Yamato, P. & Faccenna, C. Episodic slab rollback fosters exhumation of HP–UHP rocks. *Geophys. J. Int.* **179**, 1292–1300 (2009).

24. St-Onge, M.R., Rayner, N., Palin, R.M., Searle, M.P. & Waters, D.J. Integrated pressure–temperature–time constraints for the Tso Morari dome (Northwest India): implications for the burial and exhumation path of UHP units in the western Himalaya. *J. Metamorph. Geol.* **31**, 469–504 (2013).
25. Whitney, D.L. & Davis, P.B. Why is lawsonite eclogite so rare? Metamorphism and preservation of lawsonite eclogite, Sivrihisar, Turkey. *Geology* **34**, 473–476 (2006).
26. van Keken, P.E., Hacker, B.R., Syracuse, E.M. & Abers, G.A. Subduction factory: 4. Depth-dependent flux of H_2O from subducting slabs worldwide. *J. Geophys. Res*. **116**, B01401 (2011).
27. Grove, T.L., Till, C.B., Lev, E., Chatterjee, N. & Médard, E. Kinematic variables and water transport control the formation and location of arc volcanoes. *Nature* **459**, 694–697 (2009).
28. Schmidt, M.W. & Poli, S. Experimentally based water budgets for dehydrating slabs and consequences for arc magma generation. *Earth Planet. Sci. Lett.* **163**, 361–379 (1998).

Acknowledgements

Comments from B. Kaus and J. Castro (JGU Mainz) are gratefully appreciated. R. Powell (Uni. Melbourne) is thanked for providing code to calculate densities with THERMOCALC.

Author contributions

R.M.P. conceived the idea and performed the calculations. Both authors analysed the data and wrote the paper.

Competing financial interests

The authors declare no competing financial interests.

247

248 **Figure captions**

249 **Figure 1** Results of phase equilibria modelling calculations. **a**, Palaeoarchean high-MgO
250 basalt; **b**, Palaeoproterozoic olivine-bearing basalt; **c**, Mesoproterozoic gabbro; and **d**,
251 Neoproterozoic pillow basalt. Rock types are defined by assemblages listed in the Methods
252 section. Stippled regions mark glaucophane stability. Phase diagrams showing full mineral
253 assemblages calculated for each rock type are shown in Fig. S1. Actinolite differs from
254 tremolite by having molar Mg/(Mg+Fe) <0.9, and from winchite by having molar
255 Na/(Na+Ca) <0.25 in the M4 crystallographic site. Isobaric profile lines at 0.6 GPa mark the
256 greenschist-facies conditions over which actinolite compositional data shown in Fig. S3 were
257 calculated.

258

259 **Figure 2** Modebox plots of changes in calculated mineral proportions and bulk-rock density
260 during metamorphism along a warm geotherm (350 °C/GPa). **a**, Palaeoarchean high-MgO
261 basalt; **b**, Palaeoproterozoic olivine-bearing basalt; **c**, Mesoproterozoic gabbro; and **d**,
262 Neoproterozoic pillow basalt. Bulk-rock densities (g/cm^3) for each sample are represented by
263 short-dashed lines labelled $\rho_{bulk\text{-}rock}$. Vertical dashed line separating actinolite and hornblende
264 in part **c** represents the position of their solvus at the pressure–temperature conditions of
265 interest.

266

267 **Figure 3** Schematic diagrams showing the different petrological evolutions of **a**, high-MgO
268 Archean and **b**, low-MgO Neoproterozoic–modern-day oceanic crust. Isotherms are
269 qualitative and positioned in order to define a warm geotherm of 350 °C/GPa along the
270 descending slab surface. Oceanic crust is represented as being ~25–30 km thick in the
271 Archean[14] and 7 km thick in the Phanerozoic[4], although only the uppermost 5 km is assumed

to be hydrated[28] in each case. Insets show the molar percentage of H_2O released from hydrous phases during subduction (cf. Fig. S4).

Methods

Phase equilibria modelling was performed in the 10-component NCKFMASHTO (Na_2O–CaO–K_2O–FeO–MgO–Al_2O_3–SiO_2–H_2O–TiO_2–O_2) chemical system using THERMOCALC version 3.40[29] and the internally consistent thermodynamic dataset ds-55[30] (updated August 2004). A list of model parameters, activity–composition relationships for solid-solution phases, and bulk-rock compositions utilised for modelling are given in the Supplementary Information and Table S2. Rock types shown in Fig. 1 were defined according to the equilibrium (minimum Gibbs free energy) mineral assemblages calculated via modelling. The following mineral associations represent necessary constituents for each rock type: Actinolite–chlorite–lawsonite–pyroxenite = actinolite + chlorite + lawsonite + diopside/omphacite; Actinolite–chlorite–epidote–pyroxenite = actinolite + chlorite + epidote + diopside/omphacite; Epidote-blueschist = epidote + glaucophane (no lawsonite); Lawsonite-blueschist = lawsonite + glaucophane; Greenschist = albite + chlorite + actinolite; Epidote-amphibolite = epidote + hornblende + plagioclase; Epidote-hornblendeite = epidote + hornblende (no plagioclase); Hornblendite = hornblende (no plagioclase or epidote); Amphibolite = hornblende + plagioclase (no epidote); Garnet-hornblendeite = garnet + hornblende/actinolite (no plagioclase); Garnet-pyroxenite = garnet + diopside (no plagioclase); Eclogite = garnet + omphacite (no plagioclase). Note that discrimination between eclogite and garnet-pyroxenite is determined by the composition of clinopyroxene, with a sodic-calcic pyroxene (omphacite) a necessary constituent in the former, and a calcic pyroxene necessary in the latter.

Code availability: the software and datafiles used to generate the phase diagrams presented herein can be downloaded at http://www.metamorph.geo.uni-mainz.de/thermocalc/

References only in methods

29. Powell, R. & Holland, T.J.B. An internally consistent thermodynamic dataset with uncertainties and correlations: 3. Application to geobarometry, worked examples, and a computer program. *J. Metamorp. Geol.* **6**, 173–204 (1988).
30. Holland, T.J.B. & Powell, R. An internally consistent thermodynamic dataset for phases of petrological interest. *J. Metamorp. Geol.* **16**, 309–344 (1998).

Figure 1

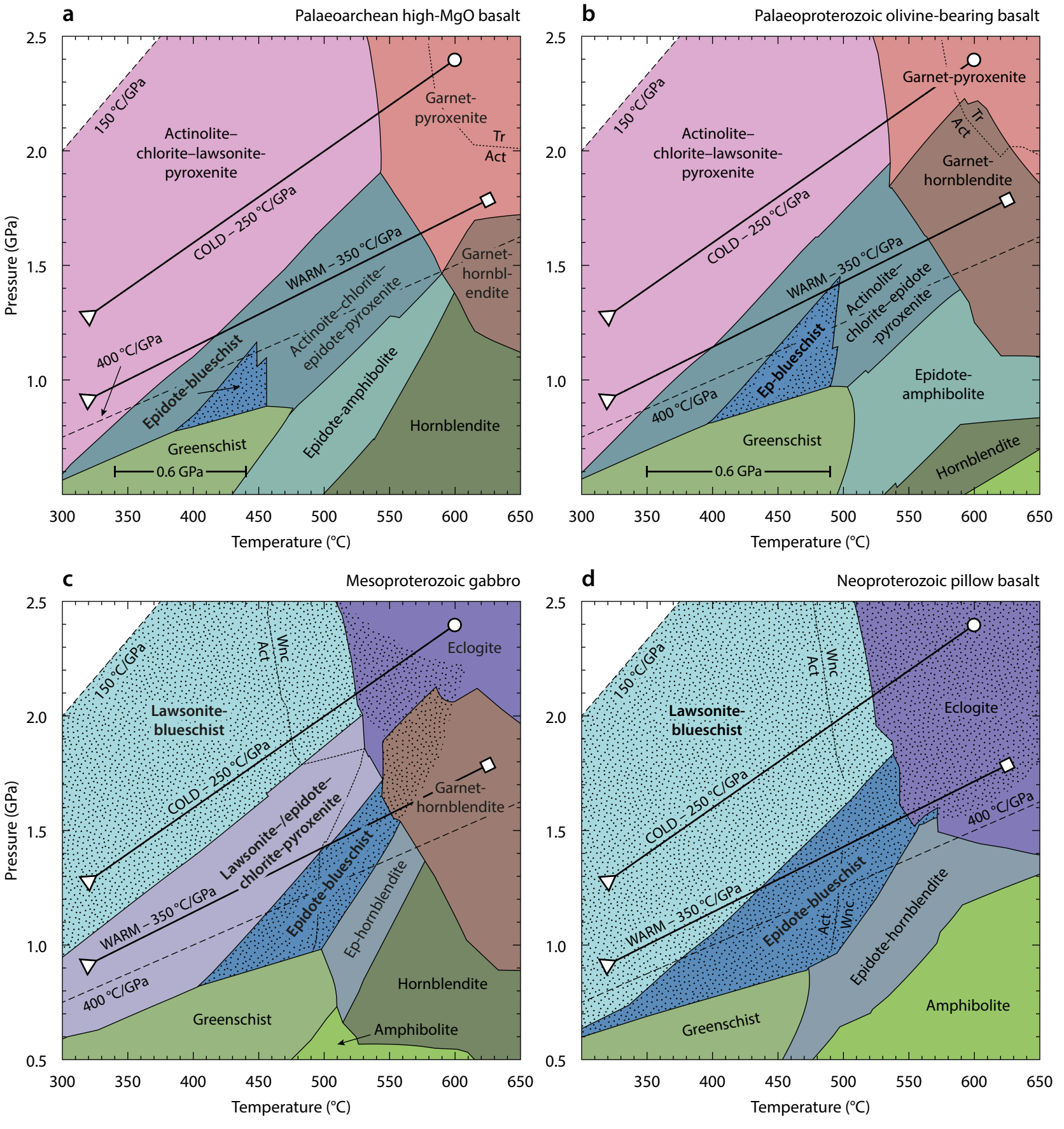
a
Palaeoarchean high-MgO basalt
b
Palaeoproterozoic olivine-bearing basalt
c
Mesoproterozoic gabbro
d
Neoproterozoic pillow basalt
Pressure (GPa)
Temperature (°C)
150 °C/GPa
400 °C/GPa
COLD – 250 °C/GPa
WARM – 350 °C/GPa
0.6 GPa
Actinolite–chlorite–lawsonite-pyroxenite
Garnet-pyroxenite
Tr
Act
Garnet-hornblendite
Actinolite–chlorite–epidote-pyroxenite
Epidote-blueschist
Ep-blueschist
Epidote-amphibolite
Greenschist
Hornblendite
Lawsonite-blueschist
Wnc
Eclogite
Lawsonite–/epidote–chlorite-pyroxenite
Ep-hornblendite
Amphibolite
Epidote-hornblendite

Figure 2

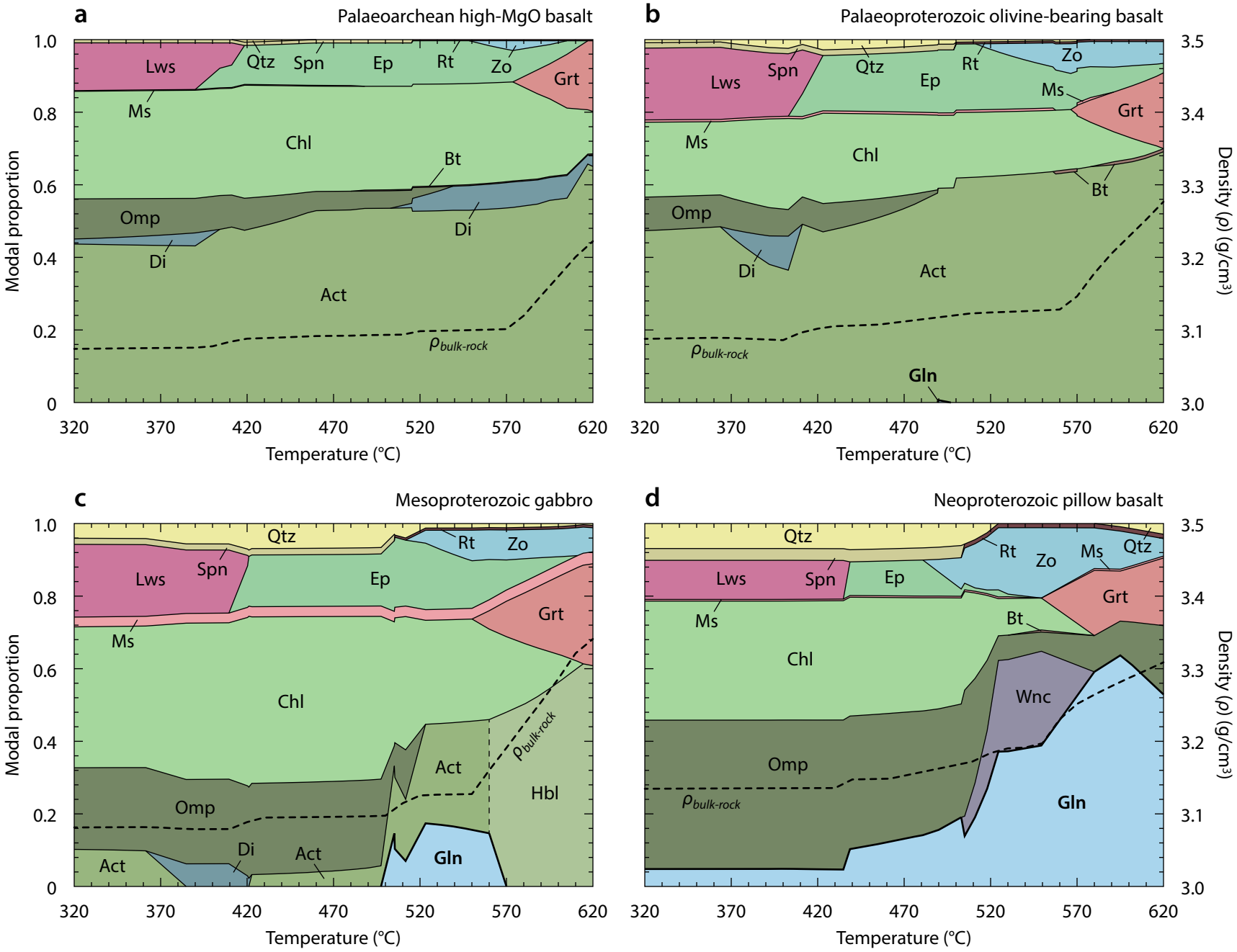
a
Palaeoarchean high-MgO basalt
b
Palaeoproterozoic olivine-bearing basalt
c
Mesoproterozoic gabbro
d
Neoproterozoic pillow basalt
Modal proportion
Density (ρ) (g/cm³)
Temperature (°C)
Lws
Qtz
Spn
Ep
Rt
Zo
Grt
Ms
Chl
Bt
Omp
Di
Act
Gln
Hbl
Wnc
ρbulk-rock

Figure 3

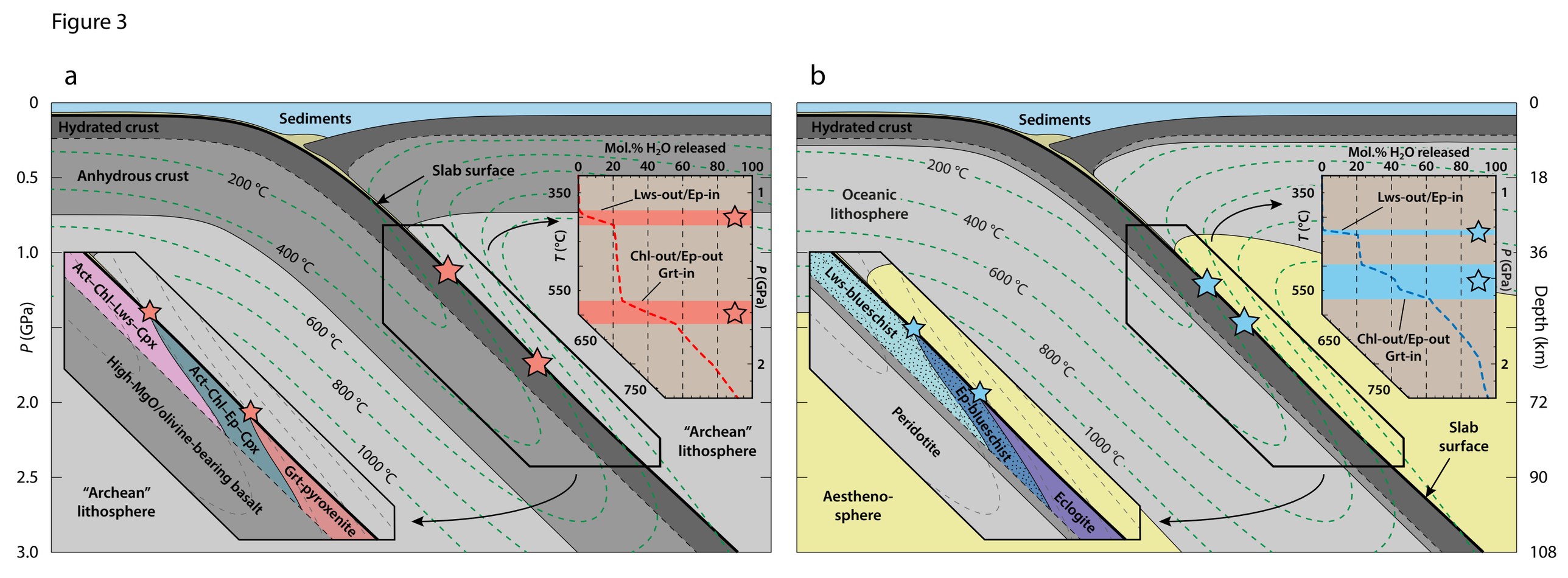
a
b
Sediments
Hydrated crust
Anhydrous crust
Slab surface
200 °C
400 °C
600 °C
800 °C
1000 °C
Act–Chl–Lws–Cpx
Act–Chl–Ep–Cpx
Grt-pyroxenite
High-MgO/olivine-bearing basalt
"Archean" lithosphere
Mol.% H2O released
0 20 40 60 80 100
T (°C)
P (GPa)
350
550
650
750
Lws-out/Ep-in
Chl-out/Ep-out
Grt-in
Oceanic lithosphere
Lws-blueschist
Ep-blueschist
Eclogite
Peridotite
Aestheno-sphere
Slab surface
Depth (km)
0
0.5
1.0
2.0
2.5
3.0
18
36
72
90
108

Emergence of blueschists on Earth linked to secular changes in oceanic crust composition

Richard M. Palin* and Richard W. White

Institute of Geosciences, Johannes-Gutenberg University Mainz, 55128 Mainz, Germany

* corresponding author: richardmpalin@gmail.com

Contents:

Early-Earth plate velocities and subduction geotherms

Early studies of Archean geodynamics initially favoured the idea that plate tectonics operated at a significantly faster rate than on the present-day Earth, purportedly owing to the dissipation of internal heat from a significantly hotter mantle being most efficient in a scenario involving rapid sea-floor spreading and subduction of relatively young (20–30 Myr) crust (e.g. Bickle, 1978; Abbott & Hoffman, 1984). Spreading rates up to ~40 cm/yr have been proposed (Dewey & Windley, 1981; Nisbet & Fowler, 1983): notably faster than the typical present-day range of 1–10 cm/yr (Solomon et al., 1975). Though some workers continue to support this 'fast-plate' hypothesis (van Krankendonk & Kirkland, 2013), the general consensus in the geological community today appears to be that plate velocities in the deep geological past were relatively more sluggish than today, though they "*should not differ greatly from that at the present*" (Korenaga, 2013). Such interpretations have been made on the basis of geological observations, with passive margins interpreted to have had longer lifespans in the Precambrian than in the Phanerozoic (Bradley, 2008), palaeomagnetic and palaeogeographic data (Condie et al., 2015), the geochemical budget of radiogenic isotope exchange between the atmosphere and Earth interior (Padhi et al., 2012), and theoretical calculations providing constraints on the evolution of the Urey ratio over time (Korenaga, 2008; Herzberg et al., 2010).

Korenaga (2006) used secular changes in mantle heat flux to predict changes in plate velocity over time, scaled against an average present-day value of 4 cm/yr. Extrapolation back to the Proterozoic–Archean boundary produced a scaled plate velocity of ~3 cm/yr, with ~2 cm/yr at the Archean–Hadean boundary. Linearly extrapolating these values against the 1–10 cm/yr present-day total range (above) leads to the conclusion that Archean subduction may have occurred at rates of ~0.5–7.5 cm/yr, with the crust being subducted having been commensurately

older (and thus colder; Korenaga, 2013) than the ~60-Myr present-day average (Bickle, 1978). The effect that slower and older descending crust may have on subduction zone thermal structure can be interpreted on a first-order basis via comparison with present-day analogues that show similar physical parameters. Investigation of slab-top pressure–temperature profiles was performed via examination of the global database compiled by Syracuse et al. (2010). For subduction zones characterised by values similar to these average "Archean" parameters (e.g. the North and South Lesser Antilles; table 2 of Syracuse et al., 2010), temperatures along the subducting slab surfaces reach ~950 °C at 2.5 GPa, but are typically lower (~700–800 °C; figs. 6 and 12 in Syracuse et al., 2010). These data define subduction geotherms of ~280–380 °C/GPa.

In conjunction with this comparative approach, we can also consider recently reported geological evidence for subduction geotherms in the early Earth. Moyen et al. (2006) and Ganne et al. (2011) identified petrological evidence in a series of high-*P* metasediments for warm subduction in the early Earth along geotherms of 10–12 °C/km – equivalent to ~350–400 °C/GPa. These data were obtained via combinations of conventional thermobarometry and phase equilibria modelling. Both studies interpreted such cool *P–T* conditions as evidence of the operation of modern-day plate tectonics and blueschist-facies metamorphism in the Archean and Proterozoic (c. 3.2 Ga and c. 2.15 Ga, respectively).

Sample selection methodology

The choice of samples employed in phase equilibria modelling was assisted by the Furnes et al. (2014) geochemical database of Precambrian greenstone belts, which utilised geochemical discrimination systematics of immobile elements (e.g. Al_2O_3, TiO_2, Zr and Ni) to classify 111 terranes distributed worldwide as having either plume, mid-ocean ridge (MOR), continental margin, volcanic arc, or suprasubduction zone affinity. In many cases, each terrane contained components showing affinities with multiple tectonic settings. Samples chosen for modelling in this work were selected based on having at least some MOR geochemical characteristics (see table 3 in Furnes et al., 2014), as such rocks are inferred to most closely reflect the evolving composition of the primitive crust throughout Earth history: a predicted consequence of secular cooling of the mantle since the Archean (cf. Herzberg et al., 2010 and see main text). Specific samples from each study were then selected based on the reported degree of alteration and/or metamorphism. Those reported to contain original igneous microstructures, macrostructures, and/or mineralogies were preferentially selected.

Phase equilibria modelling procedures

Pressure–temperature diagrams

Pseudosections were constructed using THERMOCALC v3.40 with the internally consistent thermodynamic data set ds55 (Powell and Holland, 1988; Holland and Powell, 1998; updated to August 2004). Modelling was performed in the 10-component Na_2O–CaO–K_2O–FeO–MgO–Al_2O_3–SiO_2–H_2O–TiO_2–O_2 (NCKFMASHTO) compositional system using the following activity–composition relations for solid-solution phases: glaucophane, actinolite, hornblende, cummingtonite, diopside, omphacite, and jadeite (Diener and Powell, 2012), muscovite and paragonite (Coggon and Holland, 2002), talc and epidote (Holland and Powell, 1998), chlorite (Holland et al., 1998), biotite and garnet (White et al., 2007), plagioclase and K-feldspar (Holland

and Powell, 2003), ilmenite (White et al., 2000). Pure phases included albite, zoisite, lawsonite, pumpellyite, rutile, sphene, quartz, kyanite, and H_2O. The bulk-rock compositions used for modelling were converted from weight % oxides, as reported in each original study (Table S1), to molar % oxides (Table S2). Fluid was considered to be an excess phase in all cases, owing to the observations outlined by Schmidt & Poli (1998) (and references therein) that hydrated metabasites contain approximately 5–6 wt% H_2O in the lower blueschist facies. Oxygen isotope analyses from 4.4–4.0 Ga zircons infer the existence of surface water on the early Earth (Peck et al., 2001), allowing for the interpretation that hydration of Archean oceanic crust occurred in a similar manner to that documented today. Mixed component fluids were not considered due to the lack of suitable activity models describing their behaviour at the high-*P*/low-*T* conditions under investigation. For internal consistency and ease of comparison, all calculations used a constant molar bulk-rock $Fe_2O_3/(Fe_2O_3+FeO)$ value of 0.1 (cf. Christie et al., 1986; Berry et al., 2008). Mineral abbreviations are after Kretz (1983). Pressure uncertainties for assemblage field boundaries are approximately ±1 kbar at the 2σ level (Powell & Holland, 2008; Palin et al., 2015).

H_2O-content diagram (Fig. S4)

The relative proportion of H_2O calculated to occur structurally bound within hydrous phases and as a free fluid along a warm geotherm was determined by setting water as a non-excess phase for each sample and determining the molar proportion required to achieve minimal fluid saturation at 320 °C. These values were 14.53 mol. % (4.90 wt%) for the S01 Neoproterozoic pillow basalt bulk composition and 16.31 mol. % (5.93 wt%) for the KN03 high-MgO basalt bulk composition. Both water contents lie within the typical range suggested for lower blueschist-facies hydrated oceanic crust (Schmidt & Poli, 1998). Equilibrium assemblages were then calculated along the 350 °C/GPa geotherm, which allowed determination of the proportion of water present as a free fluid phase and thus calculation of the percentage of structurally bound H_2O released during metamorphism.

Table S1 Bulk-rock compositions of mafic crustal components discussed in this work (weight % oxides).

Lithology	Reported age (Ma)	SiO_2	TiO_2	Al_2O_3	Fe_2O_3	FeO	MgO	CaO	Na_2O	K_2O
High-MgO basalt[1]	c. 3450 (Palaeoarchean)	48.75	0.48	10.32	1.21	9.81	16.19	10.49	1.42	0.03
Olivine-bearing basalt[2]	c. 1870 (Palaeoproterozoic)	49.96	0.79	11.00	1.10	8.88	14.07	11.57	1.30	0.09
Gabbro[3]	c. 1300 (Mesoproterozoic)	46.40	0.88	15.70	1.30	10.50	11.20	9.13	1.92	0.38
Pillow basalt[4]	c. 563 (Neoproterozoic)	50.33	1.61	13.49	1.12	9.05	9.66	9.22	3.59	0.06
Modern MORB[5]	c. 0–200 Ma (Phanerozoic)	50.89	1.73	14.47	1.08	8.75	8.00	10.95	2.78	0.16

N.B. Fe_2O_3 contents were calculated assuming a bulk-rock $Fe_2O_3/(FeO+Fe_2O_3) = 0.1$. [1]Kato and Nakamura (2003), sample 02MB256; [2]Hynes and Francis (1982), sample CHK-MGO14; [3]Condie and Myers (1999), sample 769; [4]Savov et al. (2001), sample BA-23; [5]Albarède (2005), average of ~5,000 mid-ocean ridge basalt glass analyses.

Table S2 Bulk-rock compositions utilised in phase equilibria modelling (molar % oxides). See Table S1 for original data sources.

Lithology	Figures	H_2O	SiO_2	Al_2O_3	CaO	MgO	FeO	K_2O	Na_2O	TiO_2	O
High-MgO basalt	1a, 2a, 3a, S1a, S2a, S3	excess	48.02	5.99	11.07	23.77	8.98	0.02	1.36	0.36	0.45
	S4	16.32	40.18	5.01	9.26	19.89	7.51	0.02	1.14	0.30	0.38
Olivine-bearing basalt	1b, 2b, S1b, S2b, S3	excess	49.77	6.46	12.35	20.89	8.22	0.06	1.26	0.59	0.41
Gabbro	1c, 2c, S1c, S2c	excess	48.77	9.72	10.28	17.55	10.26	0.26	1.96	0.70	0.51
Pillow basalt	1d, 2d, 3b, S1d, S2d	excess	52.37	8.27	10.28	14.98	8.75	0.04	3.62	1.26	0.44
	S4	14.53	44.76	7.07	8.79	12.80	7.48	0.03	3.10	1.08	0.37

Table S3 Representative compositions of actinolite calculated along various geotherms for Palaeoarchean high-MgO basalt (KN03) and Palaeoproterozoic olivine-bearing basalt (HF82) bulk-rock compositions.

		KN03 cold (250 °C/GPa) geotherm				KN03 warm (350 °C/GPa) geotherm				KN03 greenschist (0.6 GPa profile)			
Temp. (°C)		340	370	400	440	340	370	400	440	340	370	400	440
	Si	8.000	8.000	8.000	8.000	8.000	8.000	8.000	8.000	8.000	7.999	7.996	7.935
	Al	0.081	0.100	0.123	0.159	0.088	0.108	0.147	0.217	0.092	0.102	0.115	0.209
	Fe^{3+}	0.060	0.072	0.084	0.100	0.061	0.071	0.067	0.067	0.045	0.048	0.051	0.066
	Fe^{2+}	0.914	0.897	0.893	0.887	0.950	0.947	0.955	0.952	1.012	1.023	1.034	1.053
	Mg	3.946	3.933	3.904	3.862	3.902	3.875	3.834	3.771	3.852	3.828	3.806	3.742
	Ca	1.754	1.721	1.687	1.636	1.764	1.737	1.700	1.625	1.770	1.749	1.731	1.726
	Na	0.348	0.381	0.411	0.451	0.321	0.343	0.380	0.456	0.323	0.352	0.377	0.397
	Sum	15.103	15.104	15.102	15.096	15.086	15.081	15.083	15.087	15.093	15.102	15.110	15.126
	*X*Mg	0.812	0.814	0.814	0.813	0.804	0.804	0.801	0.798	0.792	0.789	0.786	0.780
T2	Si	4.000	4.000	4.000	4.000	4.000	4.000	4.000	4.000	4.000	4.000	4.000	4.000
T1	Si	4.000	4.000	4.000	4.000	4.000	4.000	4.000	4.000	4.000	3.999	3.996	3.935
	^{IV}Al	0.000	0.000	0.000	0.000	0.000	0.000	0.000	0.000	0.000	0.001	0.004	0.065
M2	^{VI}Al	0.081	0.100	0.123	0.159	0.088	0.108	0.147	0.216	0.091	0.101	0.110	0.144
	Fe^{3+}	0.060	0.072	0.084	0.100	0.061	0.071	0.067	0.067	0.045	0.048	0.051	0.066
(C site)	Fe^{2+}	0.349	0.339	0.334	0.325	0.363	0.357	0.356	0.346	0.388	0.390	0.393	0.393
	Mg	1.509	1.489	1.459	1.415	1.489	1.463	1.430	1.371	1.476	1.460	1.446	1.397
M1,3	Fe^{2+}	0.564	0.557	0.558	0.561	0.588	0.589	0.598	0.605	0.624	0.633	0.641	0.659
(C site)	Mg	2.436	2.443	2.442	2.439	2.412	2.411	2.402	2.395	2.376	2.367	2.359	2.341
	Ca	0.000	0.000	0.000	0.000	0.000	0.000	0.000	0.000	0.000	0.000	0.000	0.000
M4	Fe^{2+}	0.000	0.000	0.001	0.002	0.000	0.000	0.001	0.001	0.000	0.000	0.000	0.001
	Mg	0.001	0.002	0.003	0.007	0.001	0.001	0.002	0.004	0.000	0.001	0.001	0.003
(B site)	Ca	1.754	1.721	1.687	1.636	1.764	1.737	1.700	1.625	1.770	1.749	1.731	1.726
	Na	0.245	0.277	0.309	0.355	0.235	0.261	0.297	0.369	0.230	0.251	0.267	0.271
A site	Na	0.103	0.104	0.102	0.096	0.086	0.081	0.083	0.087	0.093	0.102	0.110	0.126
	vac	0.897	0.896	0.898	0.904	0.914	0.919	0.917	0.913	0.907	0.898	0.890	0.874

Table S3 (continued)

		HF82 cold (250 °C/GPa) geotherm					HF82 warm (350 °C/GPa) geotherm					HF82 greenschist (0.6 GPa profile)				
Temp. (°C)		350	380	410	440	490	350	380	410	440	490	350	380	410	440	490
	Si	8.000	8.000	8.000	8.000	8.000	8.000	8.000	8.000	8.000	7.996	8.000	7.999	7.998	7.990	7.899
	Al	0.122	0.131	0.139	0.156	0.208	0.099	0.116	0.159	0.219	0.332	0.095	0.103	0.113	0.131	0.272
	Fe^{3+}	0.102	0.108	0.110	0.118	0.131	0.071	0.075	0.066	0.052	0.067	0.039	0.041	0.043	0.045	0.057
	Fe^{2+}	1.027	1.026	1.023	1.020	1.011	1.049	1.017	1.033	1.013	1.042	1.092	1.101	1.109	1.117	1.133
	Mg	3.751	3.739	3.734	3.716	3.674	3.782	3.794	3.746	3.722	3.577	3.775	3.757	3.740	3.721	3.653
	Ca	1.671	1.660	1.651	1.628	1.554	1.747	1.727	1.690	1.638	1.504	1.786	1.781	1.777	1.773	1.780
	Na	0.429	0.435	0.437	0.451	0.506	0.333	0.351	0.389	0.444	0.572	0.294	0.292	0.289	0.286	0.285
	Sum	15.103	15.098	15.094	15.088	15.083	15.081	15.080	15.082	15.087	15.091	15.080	15.074	15.069	15.065	15.079
	*X*Mg	0.785	0.785	0.785	0.785	0.784	0.783	0.789	0.784	0.786	0.774	0.776	0.773	0.771	0.769	0.763
T2	Si	4.000	4.000	4.000	4.000	4.000	4.000	4.000	4.000	4.000	4.000	4.000	4.000	4.000	4.000	4.000
T1	Si	4.000	4.000	4.000	4.000	4.000	4.000	4.000	4.000	4.000	3.996	4.000	3.999	3.998	3.990	3.899
	^{IV}Al	0.000	0.000	0.000	0.000	0.000	0.000	0.000	0.000	0.000	0.004	0.000	0.001	0.002	0.010	0.101
M2	^{VI}Al	0.122	0.131	0.139	0.156	0.208	0.099	0.116	0.158	0.218	0.328	0.095	0.103	0.111	0.121	0.171
	Fe^{3+}	0.102	0.108	0.110	0.118	0.131	0.071	0.075	0.066	0.052	0.067	0.039	0.041	0.043	0.045	0.057
(C site)	Fe^{2+}	0.382	0.379	0.377	0.372	0.358	0.397	0.382	0.384	0.370	0.362	0.419	0.421	0.422	0.423	0.419
	Mg	1.394	1.382	1.375	1.354	1.303	1.433	1.427	1.392	1.360	1.243	1.448	1.435	1.424	1.410	1.352
M1,3	Fe^{2+}	0.645	0.646	0.645	0.646	0.647	0.651	0.634	0.648	0.642	0.677	0.673	0.680	0.686	0.693	0.710
(C site)	Mg	2.355	2.354	2.355	2.354	2.353	2.349	2.366	2.352	2.358	2.323	2.327	2.320	2.314	2.307	2.290
	Ca	0.000	0.000	0.000	0.000	0.000	0.000	0.000	0.000	0.000	0.000	0.000	0.000	0.000	0.000	0.000
M4	Fe^{2+}	0.000	0.001	0.001	0.002	0.005	0.000	0.000	0.001	0.001	0.003	0.000	0.000	0.001	0.001	0.003
	Mg	0.001	0.003	0.005	0.008	0.018	0.001	0.001	0.003	0.004	0.011	0.001	0.001	0.002	0.004	0.011
(B site)	Ca	1.671	1.660	1.651	1.628	1.554	1.747	1.727	1.690	1.638	1.504	1.786	1.781	1.777	1.773	1.780
	Na	0.327	0.337	0.343	0.362	0.422	0.251	0.271	0.307	0.357	0.482	0.214	0.218	0.220	0.221	0.206
A site	Na	0.103	0.098	0.094	0.088	0.083	0.081	0.080	0.082	0.087	0.091	0.080	0.074	0.069	0.065	0.079
	vac	0.897	0.902	0.906	0.912	0.917	0.919	0.920	0.918	0.913	0.909	0.920	0.926	0.931	0.935	0.921

Figure S1a

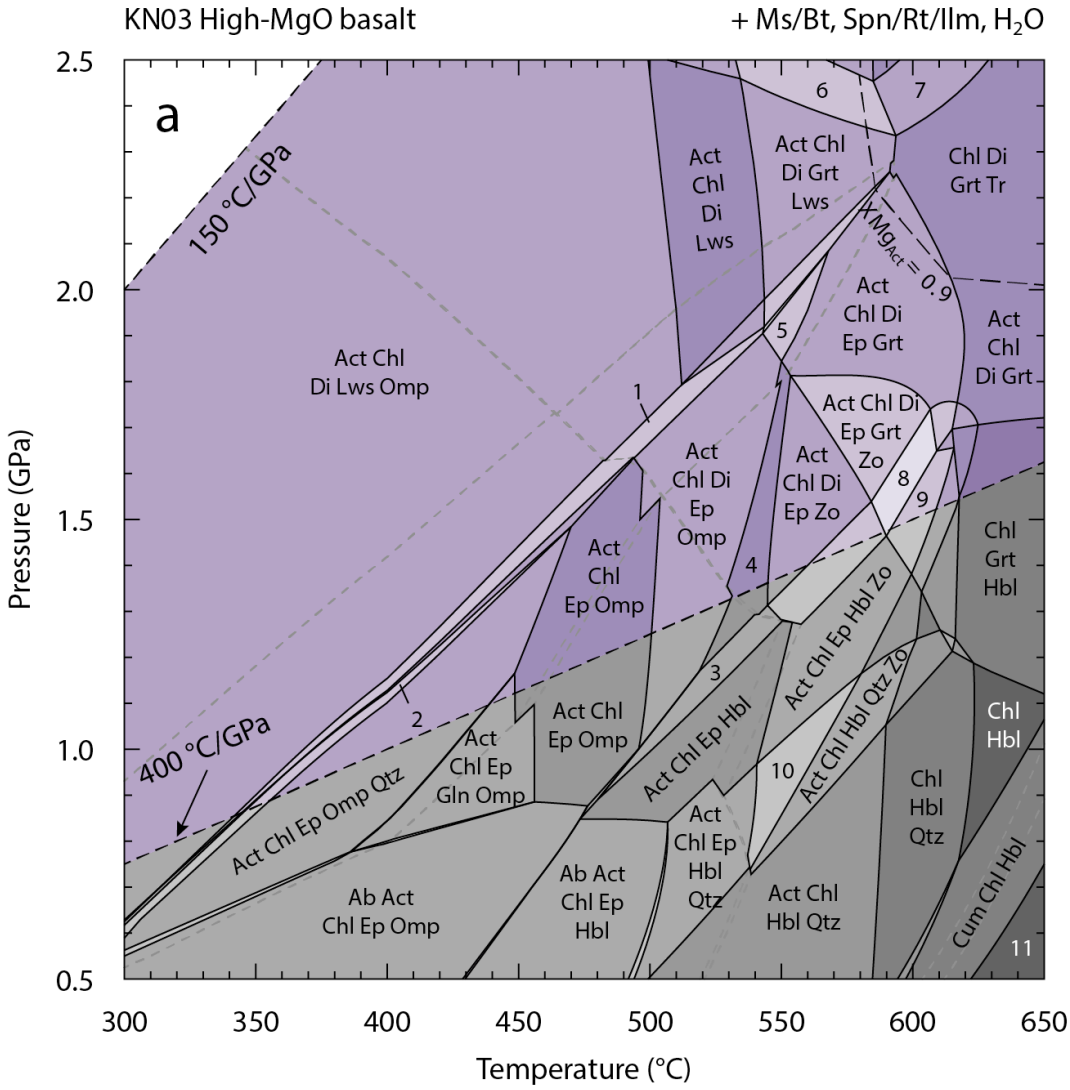

Pressure–temperature (*P*–*T*) pseudosection calculated for the bulk-rock composition (Table S2) of Palaeoarchean high-MgO basalt sample 02MB256 from Kato and Nakamura (2003). Phase assemblage fields correspond to those shown in Fig. 1a in the main manuscript. Dashed line labelled $X\mathrm{Mg}_{\mathrm{Act}} = 0.9$ marks the division between actinolite (<0.9) at low-*T*/low-*P* and tremolite (>0.9) at high-*T*/high-*P*. Some small, minor fields are unlabelled for clarity. Assemblage field boundaries marking the appearance or disappearance of muscovite, biotite, sphene, ilmenite, or rutile, are shown as grey dashed lines, which are omitted from the labelled assemblages due to their negligible calculated modal proportions (Fig. S2). Numbered fields are as follows: 1 – Act Chl Di Ep Lws Omp, 2 – Act Chl Ep Lws Omp Qtz, 3 – Act Chl Di Ep Hbl, 4 – Act Chl Di Ep, 5 – Act Chl Di Ep Grt Omp, 6 – Act Chl Di Grt Lws Tlc, 7 – Act Chl Di Grt Tlc, 8 – Act Chl Di Ep Grt Hbl Zo, 9 – Act Chl Ep Grt Hbl Zo, 10 – Act Chl Ep Hbl Qtz Zo, 11 – Cum Hbl.

Figure S1b

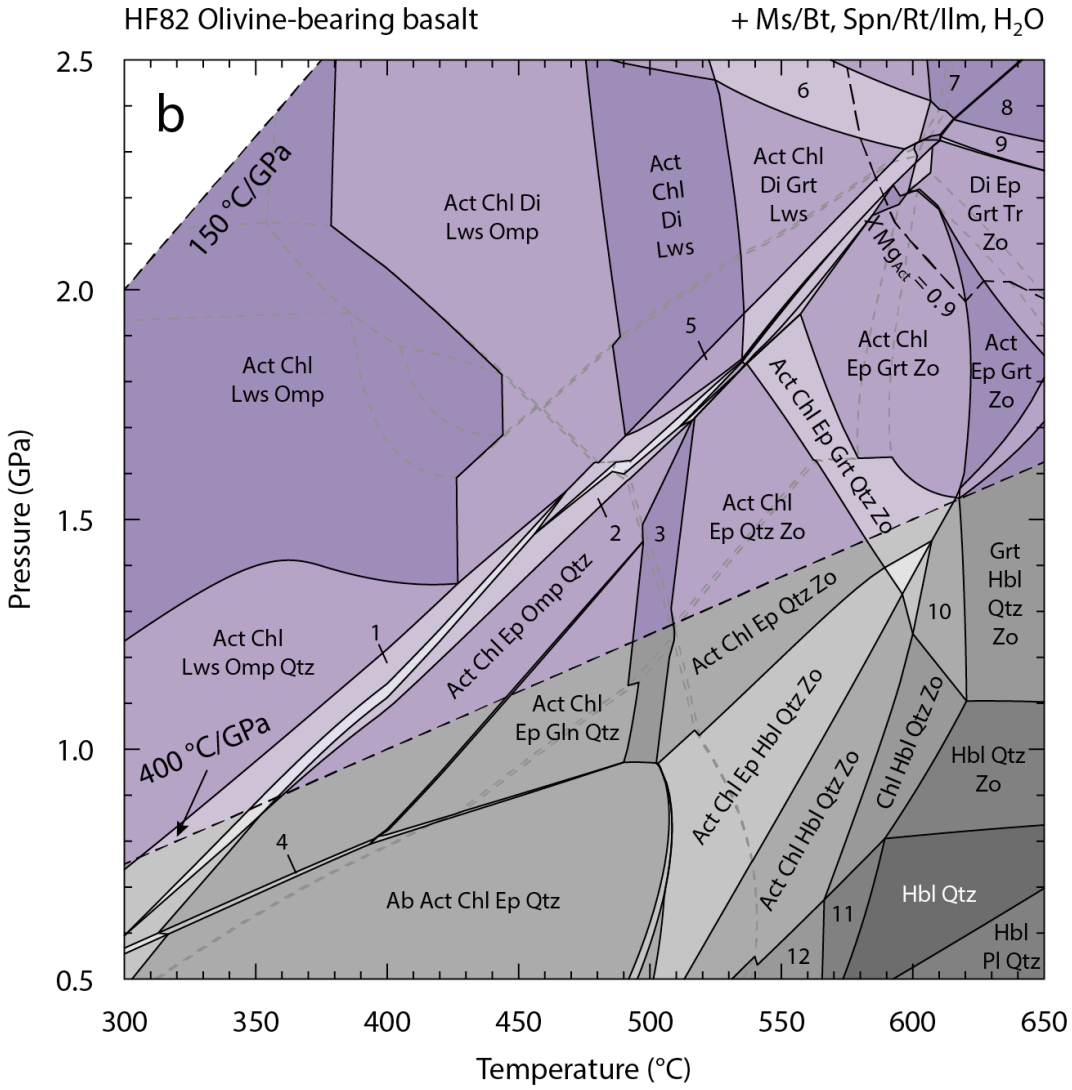

Pressure–temperature (*P*–*T*) pseudosection calculated for the bulk-rock composition (Table S2) of Palaeoproterozoic olivine-bearing basalt sample CHK-MGO14 from Hynes and Francis (1982). Phase assemblage fields correspond to those shown in Fig. 1b in the main manuscript. Dashed line labelled $X\mathrm{Mg}_{\mathrm{Act}}$ = 0.9 marks the division between actinolite (<0.9) at low-*T*/low-*P* and tremolite (>0.9) at high-*T*/high-*P*. Some small, minor fields are unlabelled for clarity. Assemblage field boundaries marking the appearance or disappearance of muscovite, biotite, sphene, ilmenite, or rutile, are shown as grey dashed lines, which are omitted from the labelled assemblages due to their negligible calculated modal proportions (Fig. S2). Numbered fields are as follows: 1 – Act Chl Di Lws Omp Qtz, 2 – Act Chl Ep Lws Omp Qtz, 3 – Act Chl Ep Qtz, 4 – Ab Act Chl Ep Omp Qtz, 5 – Act Chl Di Ep Lws, 6 – Act Chl Di Grt Lws Tlc, 7 – Di Grt Lws Tlc, 8 – Di Grt Tlc Zo, 9 – Act Di Grt Tlc Zo, 10 – Chl Grt Hbl Qtz Zo, 11 – Chl Hbl Qtz, 12 – Act Chl Hbl Qtz.

Figure S1c

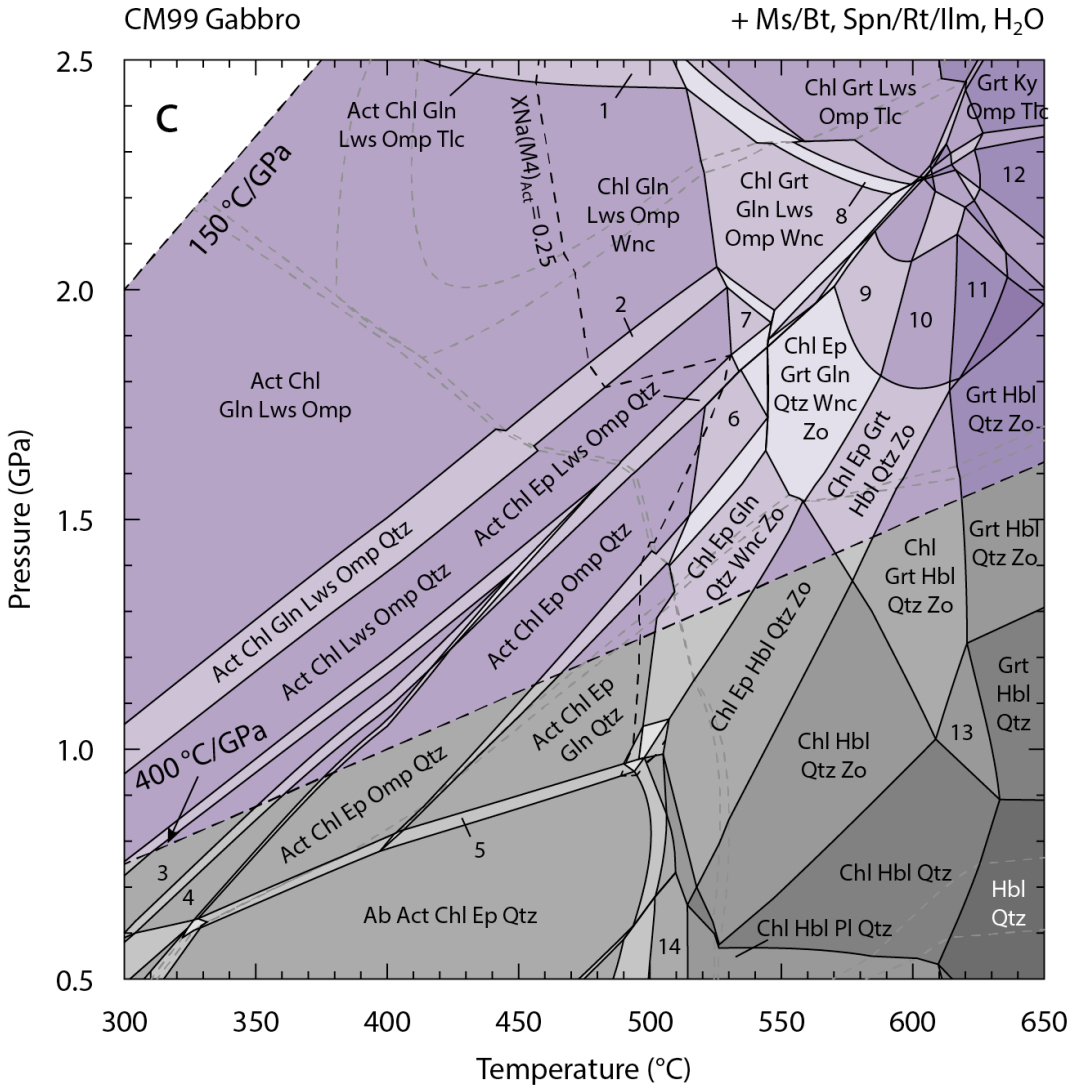

Pressure–temperature (*P*–*T*) pseudosection calculated for the bulk-rock composition (Table S2) of Mesoproterozoic gabbro sample 769 from Condie and Myers (1999). Phase assemblage fields correspond to those shown in Fig. 1c in the main manuscript. Dashed line labelled $X\text{Na(M4)}_{\text{Act}} = 0.25$ marks the division between actinolite (<0.25) at low-*T*/low-*P* and winchite (>0.25) at high-*T*/high-*P*. Some small, minor fields are unlabelled for clarity. Assemblage field boundaries marking the appearance or disappearance of muscovite, biotite, sphene, ilmenite, or rutile, are shown as grey dashed lines, which are omitted from the labelled assemblages due to their negligible calculated modal proportions (Fig. S2). Numbered fields are as follows: 1 – Chl Gln Lws Omp Tlc Wnc, 2 – Chl Ep Gln Lws Omp Wnc, 3 – Chl Di Lws Omp Qtz, 4 – Chl Di Ep Omp Qtz, 5 – Ab Act Chl Ep Gln Qtz, 6 – Act Chl Ep Omp Qtz Zo, 7 – Act Chl Gln Grt Lws Omp Qtz, 8 – Chl Grt Gln Lws Omp Tlc Wnc, 9 – Chl Ep Grt Gln Wnc Zo, 10 – Chl Ep Grt Wnc Zo, 11 – Ep Grt Wnc Zo, 12 – Grt Ky Omp Wnc, 13 – Chl Grt Hbl Qtz, 14 – Chl Ep Hbl Pl Qtz.

Figure S1d

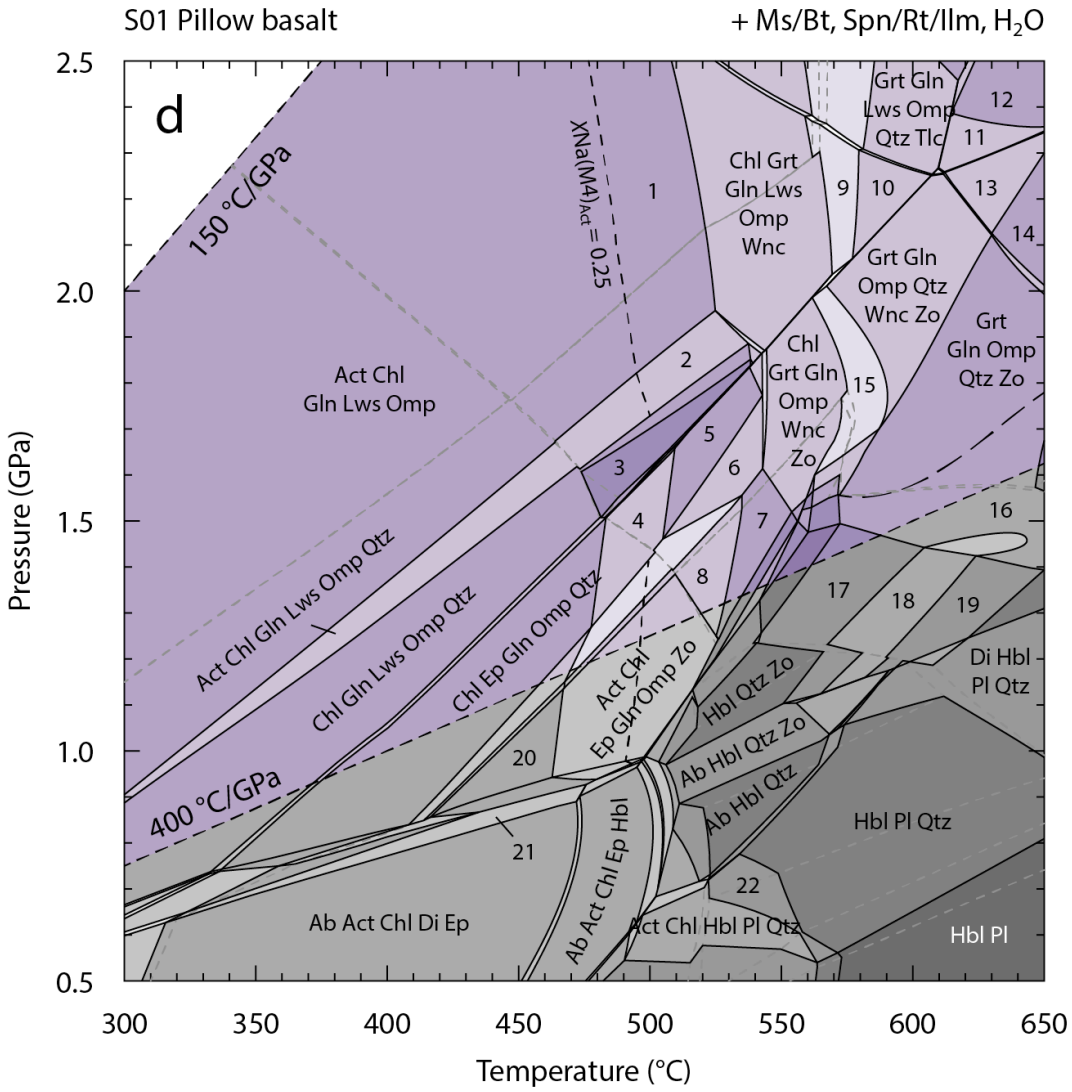

Pressure–temperature (*P*–*T*) pseudosection calculated for the bulk-rock composition (Table S2) of Neoproterozoic pillow basalt sample BA-23 from Savov et al. (2001). Phase assemblage fields correspond to those shown in Fig. 1d in the main manuscript. Dashed line labelled $X\text{Na(M4)}_{\text{Act}}$ = 0.25 marks the division between actinolite (<0.25) at low-*T*/low-*P* and winchite (>0.25) at high-*T*/high-*P*. The long-dashed line at 1.5–1.7 GPa and 550–650 °C marks the Hbl–Gln solvus extension. Some small, minor fields are unlabelled for clarity. Assemblage field boundaries marking the appearance or disappearance of muscovite, biotite, sphene, ilmenite, or rutile, are shown as grey dashed lines, which are omitted from the labelled assemblages due to their negligible calculated modal proportions (Fig. S5). Numbered fields are as follows: 1 – Wnc Chl Gln Lws Omp, 2 – Wnc Chl Gln Lws Omp Qtz, 3 – Gln Lws Omp Qtz, 4 – Chl Ep Gln Omp Qtz Zo, 5 – Chl Gln Omp Qtz Zo, 6 – Chl Gln Omp Qtz Wnc Zo, 7 – Chl Gln Omp Wnc Zo, 8 – Chl Gln Omp Wnc, 9 – Chl Grt Gln Lws Omp Wnc Qtz, 10 –Grt Gln Lws Omp Wnc Qtz, 11 – Grt Gln Ky Omp Qtz Tlc, 12 – Grt Ky Omp Qtz Tlc, 13 – Grt Gln Ky Omp Qtz Wnc, 14 – Grt Gln Ky Omp Qtz, 15 – Chl Grt Gln Omp Qtz Wnc Zo, 16 – Grt Hbl Omp Qtz Zo, 17 – Hbl Omp Qtz Zo, 18 – Di Hbl Omp Qtz Zo, 19 – Di Hbl Qtz Zo, 20 – Act Chl Ep Gln Omp, 21 – Ab Act Chl Di Ep Gln, 22 – Act Hbl Pl Qtz.

Figure S2

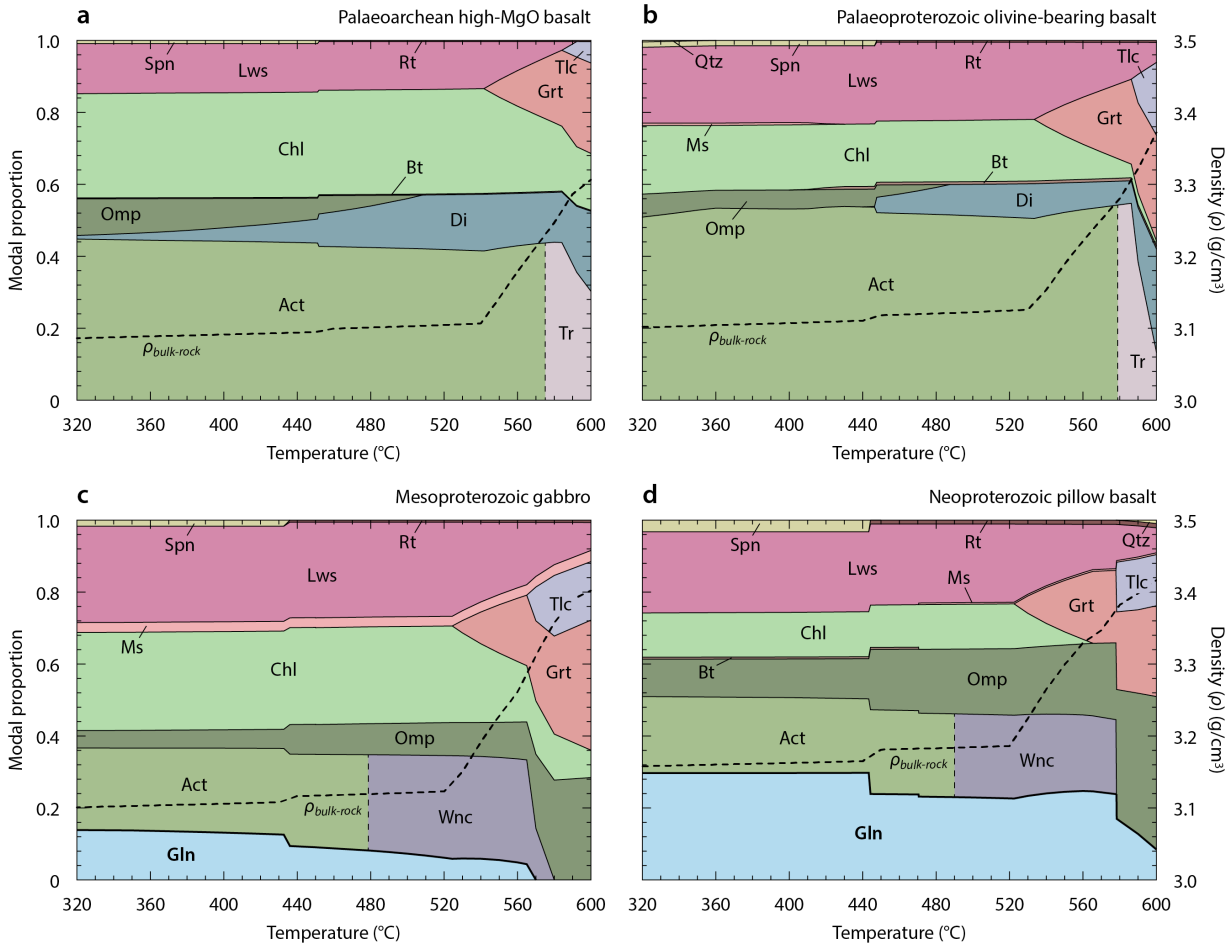

Modebox plots showing the changes in calculated mineral proportions and bulk-rock density during metamorphism along a cold geotherm (250 °C/GPa). **a**, Palaeoarchean high-MgO basalt sample 02MB256 (Kato and Nakamura, 2003); **b**, Palaeoproterozoic olivine-bearing basalt sample CHK-MGO14 (Hynes and Francis, 1982); **c**, Mesoproterozoic gabbro sample 769 (Condie and Myers, 1999); and **d**, Neoproterozoic pillow basalt sample BA-23 (Savov et al., 2001). Mineral abbreviations are after Kretz (1983). Bulk-rock density (g/cm^3) is represented by a short-dashed line in each plot. Dashed line separating actinolite and tremolite in parts **a** and **b** represents the compositional isopleth $X\mathrm{Mg}_{\mathrm{Act}}$ = 0.9, with actinolite having <0.9 and tremolite having >0.9. Dashed line separating actinolite and winchite in parts **c** and **d** represents the compositional isopleth $X\mathrm{Na(M4)}_{\mathrm{Act}}$ = 0.25, with actinolite having <0.25 and winchite having >0.25.

Figure S3

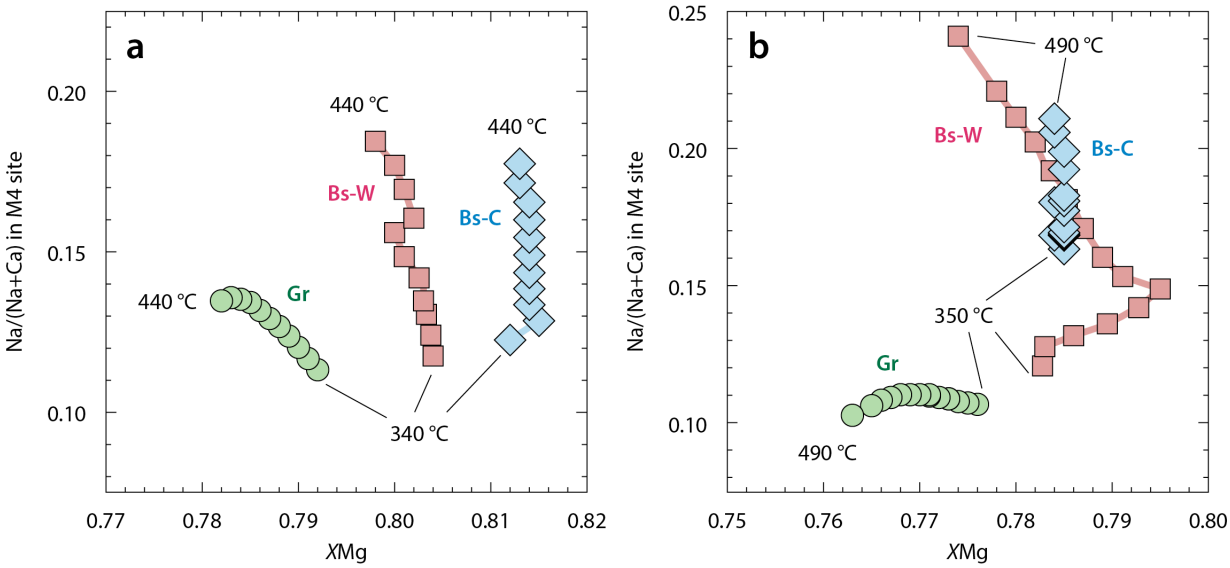

Calculated compositions of actinolite at different pressure–temperature conditions for **a**, Palaeoarchean high-MgO basalt and **b**, Palaeoproterozoic olivine-bearing basalt bulk-rock compositions. Abbreviations are as follows: Bs-C = Blueschist-facies cold geotherm (250 °C/GPa; diamonds), Bs-W = Blueschist-facies warm geotherm (350 °C/GPa; squares), Gr = Greenschist facies (0.6 GPa; circles). Symbols denote compositions at 10 °C intervals along each profile. Na/(Na+Ca) in the M4 crystallographic site represents the proportion of "glaucophane" in the amphibole structure (Leake et al., 1997) and *X*Mg = Mg/(Fe^{2+}+Mg). Representative compositions are given in Table S3.

Figure S4

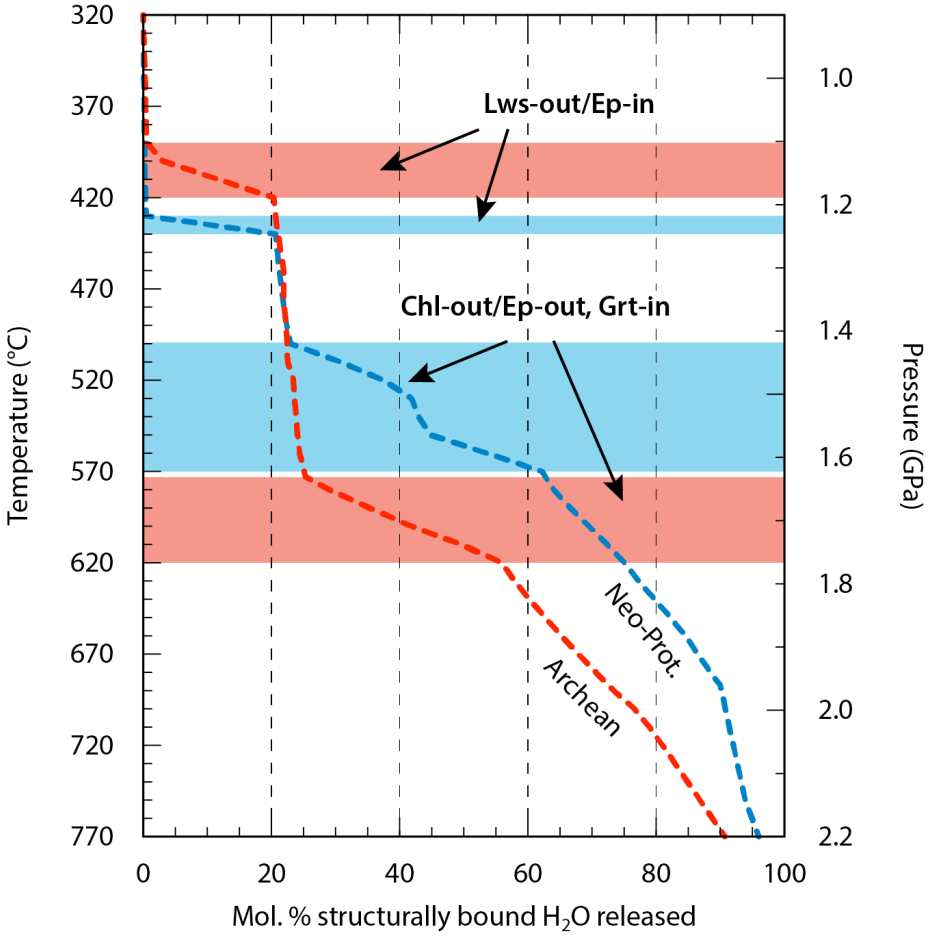

Pressure–temperature (*P–T*) plot showing the molar percent of structurally bound H_2O released during prograde metamorphism along a warm geotherm (350 °C/GPa). Samples comprise the Palaeoarchean high-MgO basalt composition of Kato and Nakamura (2003) (red dashed line labelled Archean), and the Neoproterozoic pillow basalt composition of Savov et al. (2001) (blue dashed line labelled Neo-Prot.). Red and blue horizontal bands represent approximate *P–T* ranges over which important dehydration reactions occur for each sample. Percentages are normalized against the minimum absolute number of moles of H_2O required to saturate the calculated equilibrium solid assemblage at 320 °C and 9.1 kbar (the first *P–T* point along the calculated geotherm). These absolute values were calculated to be 16.3 and 14.5 mol. % H_2O (5.93 and 4.90 wt%) for the Archean high-MgO basalt and the Neoproterozoic pillow basalt, respectively. As such, the high-MgO basalt has the potential to hold ~20% more structurally bound H_2O in its bulk-rock composition than the Neoproterozoic basalt under equivalent fluid-saturated conditions.

References

Abbott, D.H. & Hoffman, S.E. Archaean plate tectonics revisited 1. Heat flow, spreading rate, and the age of subducting oceanic lithosphere and their effects on the origin and evolution of continents. *Tectonics* **3**, 429–448.

Albarède, F. The survival of mantle geochemical heterogeneities. In van der Hilst, R., et al., eds, *Structure, Composition, and Evolution of Earth's Mantle*. Geophysical Monograph of the American Geophysical Union **160**, 27–46 (2005).

Berry, A.J., Danyushevsky, L.V., O'Neill, H. St C., Newville, M. & Sutton, S.R. Oxidation state of iron in komatiitic melt inclusions indicates hot Archaean mantle. *Nature* **455**, 960–963 (2008).

Bickle, M.J. Heat loss from the earth: A constraint on Archean plate tectonics from the relation between geothermal gradients and the rate of plate production. *Earth Planet. Sci. Lett.* **40**, 301–315 (1978).

Bradley, D.C. Passive margins through earth history. *Earth-Sci. Rev.* **91**, 1–26 (2008).

Christie, D.M., Carmichael, I.S.E. & Langmuir, C.H. Oxidation states of mid-ocean ridge basalt glasses. *Earth Planet. Sci. Lett.* **79**, 397–411 (1986).

Coggon, R. & Holland, T.J.B. Mixing properties of phengitic micas and revised garnet-phengite thermobarometers. *J. Metamorp. Geol.* **20**, 683–696 (2002).

Condie, K.C. & Myers, J.S. Mesoproterozoic Fraser Complex: geochemical evidence for multiple subduction-related sources of lower crustal rocks in the Albany–Fraser Orogen, Western Australia. *Aust. J. Earth Sci.* **46**, 875–882 (1999).

Condie, K.C., Pisarevsky, S.A., Korenega, J. & Gardoll, S. Is the rate of supercontinent assembly changing with time? *Precambrian Res.* **259**, 278–289 (2015).

Dewey, J.F. & Windley, B.F. Growth and differentiation of continental crust. *Philos. T. R. Soc. Lond. S-A.* **301**, 189–206 (1981).

Diener, J.F.A. & Powell, R. Revised activity–composition models for clinopyroxene and amphibole. *J. Metamorp. Geol.* **30**, 131–142 (2012).

Furnes, H., Dilek, Y. & de Wit, M. Precambrian greenstone sequences represent different ophiolite types. *Gondwana Res.* **27**, 649–685 (2014).

Ganne, J., et al. Modern-style plate subduction preserved in the Palaeoproterozoic West African craton. *Nature Geosci.* **5**, 60–65 (2011).

Herzberg, C., Condie, K. & Korenaga, J. Thermal history of the Earth and its petrological expression. *Earth Planet. Sci. Lett.* **292**, 79–88 (2010).

Holland, T.J.B. & Powell, R. An internally-consistent thermodynamic dataset for phases of petrological interest. *J. Metamorp. Geol.* **16**, 309–344 (1998).

Holland, T.J.B. & Powell, R. Activity-composition relations for phases in petrological calculations: an asymmetric multicomponent formulation. *Contrib. Mineral. Petrol.* **145**, 492–501 (2003).

Holland, T.J.B., Baker, J.M. & Powell, R. Mixing properties and activity–composition relationships of chlorites in the system MgO–FeO–Al_2O_3–SiO_2–H_2O. *Eur. J. Mineral.* **10**, 395–406 (1998).

Hynes, A.J. & Francis, D.M. A transect of the early Proterozoic Cape Smith foldbelt, New Quebec. *Tectonophysics* **88**, 23–59 (1982).

Kato, Y. & Nakamura, K. Origin and global tectonic significance of Early Archean cherts from the Marble Bar greenstone belt, Pilbara Craton, Western Australia. *Precambrian Res.* **125**, 191–243 (2003).

Korenaga, J. Archean geodynamics and the thermal evolution of Earth. In Benn, K. et al., eds, *Archean Geodynamics and Environments*. American Geophysical Union, Washington, D.C. (2006).

Korenaga, J. Urey Ratio and the structure and evolution of the Earth's mantle. *Rev. Geophys.* **46**, RG2007 (2008).

Korenaga, J. Initiation and evolution of plate tectonics on Earth: Theories and observations. *Annu. Rev. Earth Sci.* **41**, 117–51 (2013).

Kretz, P. Symbols for rock-forming minerals. *Am. Mineral.* **68**, 277–279 (1983).

Leake, B.E. et al. Nomenclature of amphiboles: Report of the Subcommittee on Amphiboles of the International Mineralogical Association, Commission on New Minerals and Mineral Names. *Am. Mineral.* **82**, 1019–1037 (1997).

Moyen, J.F., Stevens, G. & Kisters, A. Record of mid-Archaean subduction from metamorphism in the Barbeton terrain, South Africa. *Nature* **442**, 559–562 (2006).

Nisbet, E.G. & Fowler, C.M.R. Model for Archean plate tectonics. *Geology* **11**, 376–379 (1983).

Padhi, C., Korenaga, J. & Ozima, M. Thermal evolution of Earth with xenon degassing: a self-consistent approach. *Earth Planet. Sci. Lett*. **1–9**, 341–344, (2012)

Palin, R.M., Weller, O.M., Waters, D.J. & Dyck, B. Quantifying geological uncertainty in metamorphic phase equilibria modelling; a Monte Carlo assessment and implications for tectonic interpretations. *Geosci. Front. (in press)*, doi: 10.1016/j.gsf.2015.08.005.

Peck, W.H., Valley, J.W., Wilde, S.A. & Graham, C.M. Oxygen isotope ratios and rare earth elements in 3.3 to 4.4 Ga zircons: Ion microprobe evidence for high $\delta^{18}O$ continental crust and oceans in the Early Archean. *Geochim. Cosmochim. Acta* **65**, 4215–4229 (2001).

Powell, R. & Holland, T.J.B. An internally consistent thermodynamic dataset with uncertainties and correlations: 3. Application to geobarometry, worked examples, and a computer program. *J. Metamorp. Geol.* **6**, 173–204 (1988).

Powell, R. & Holland, T.J.B. On thermobarometry. *J. Met. Geol.* **26**, 155–179 (2008).

Savov, I., Ryan, J., Haydoutov, I. & Schijf, J. Late Precambrian Balkan-Carpathian ophiolite – a slice of the Pan-African ocean crust? Geochemical and tectonic insights from the Tcherni Vrah and Deli Jovan massifs, Bulgaria and Serbia. *J. Volcanol. Geoth. Res.* **110**, 299–318 (2001).

Schmidt, M.W., & Poli, S. Experimentally based water budgets for dehydrating slabs and consequences for arc magma generation. *Earth Planet. Sci. Lett.* **163**, 361–379 (1998).

Solomon, S.C., Sleep, N.H. & Richardson, R.M. On the forces driving plate tectonics: Inferences from absolute plate velocities and intraplate stress. *Geophys. J. Roy. Astr. S.* **42**, 769–801 (1975).

Syracuse, E.M., van Keken, P.E. & Abers, G.A. The global range of subduction zone thermal models. *Phys. Earth Planet. In.* **183**, 73–90 (2010).

Van Krankendonk, M.J. & Kirkland, C.L. Orogenic climax of Earth: The 1.2–1.1 Ga Grenvillian superevent. *Geology* **7**, 735–738 (2013).

White, R.W., Powell, R., Holland, T.J.B. & Worley, B.A. The effect of TiO_2 and Fe_2O_3 on metapelitic assemblages at greenschist and amphibolite facies conditions: mineral equilibria calculations in the system K_2O–FeO–MgO–Al_2O_3–SiO_2–H_2O–TiO_2–Fe_2O_3. *J. Metamorp. Geol.* **18**, 497–511 (2000).

White, R.W., Powell, R. & Holland, T.J.B. Progress relating to calculation of partial melting equilibria for metapelites. *J. Metamorp. Geol.* **25**, 511–527 (2007).

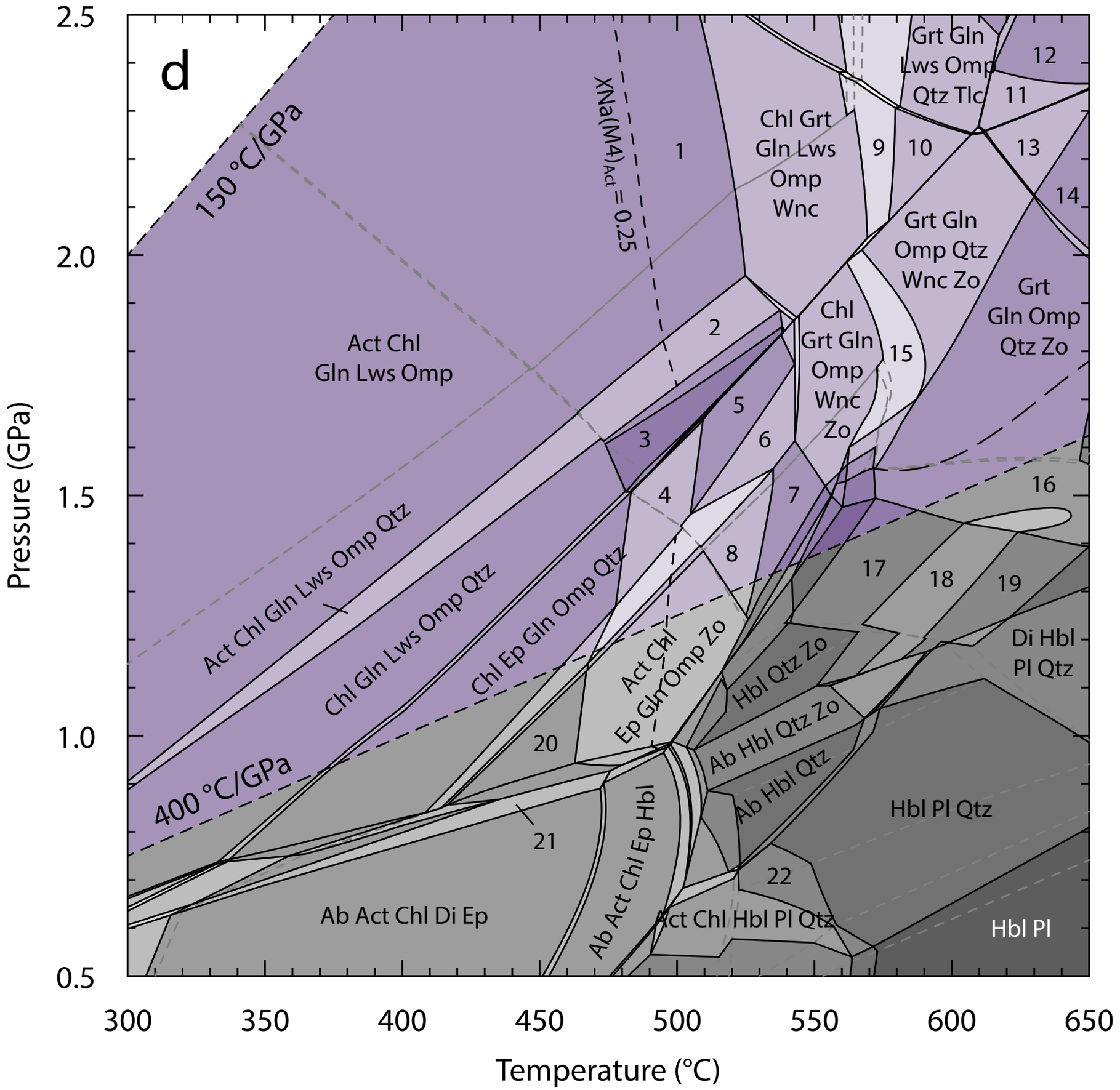
S01 Pillow basalt
+ Ms/Bt, Spn/Rt/Ilm, H2O
d
150 °C/GPa
400 °C/GPa
XNa(M4)Act = 0.25
1
2
3
4
5
6
7
8
9
10
11
12
13
14
15
16
17
18
19
20
21
22
Act Chl Gln Lws Omp
Chl Grt Gln Lws Omp Wnc
Grt Gln Lws Omp Qtz Tlc
Grt Gln Omp Qtz Wnc Zo
Chl Grt Gln Omp Wnc Zo
Grt Gln Omp Qtz Zo
Act Chl Gln Lws Omp Qtz
Chl Gln Lws Omp Qtz
Chl Ep Gln Omp Qtz
Act Chl Ep Gln Omp Zo
Hbl Qtz Zo
Ab Hbl Qtz Zo
Ab Hbl Qtz
Di Hbl Pl Qtz
Hbl Pl Qtz
Ab Act Chl Ep Hbl
Ab Act Chl Di Ep
Act Chl Hbl Pl Qtz
Hbl Pl
Pressure (GPa)
2.5
2.0
1.5
1.0
0.5
300
350
400
450
500
550
600
650
Temperature (°C)

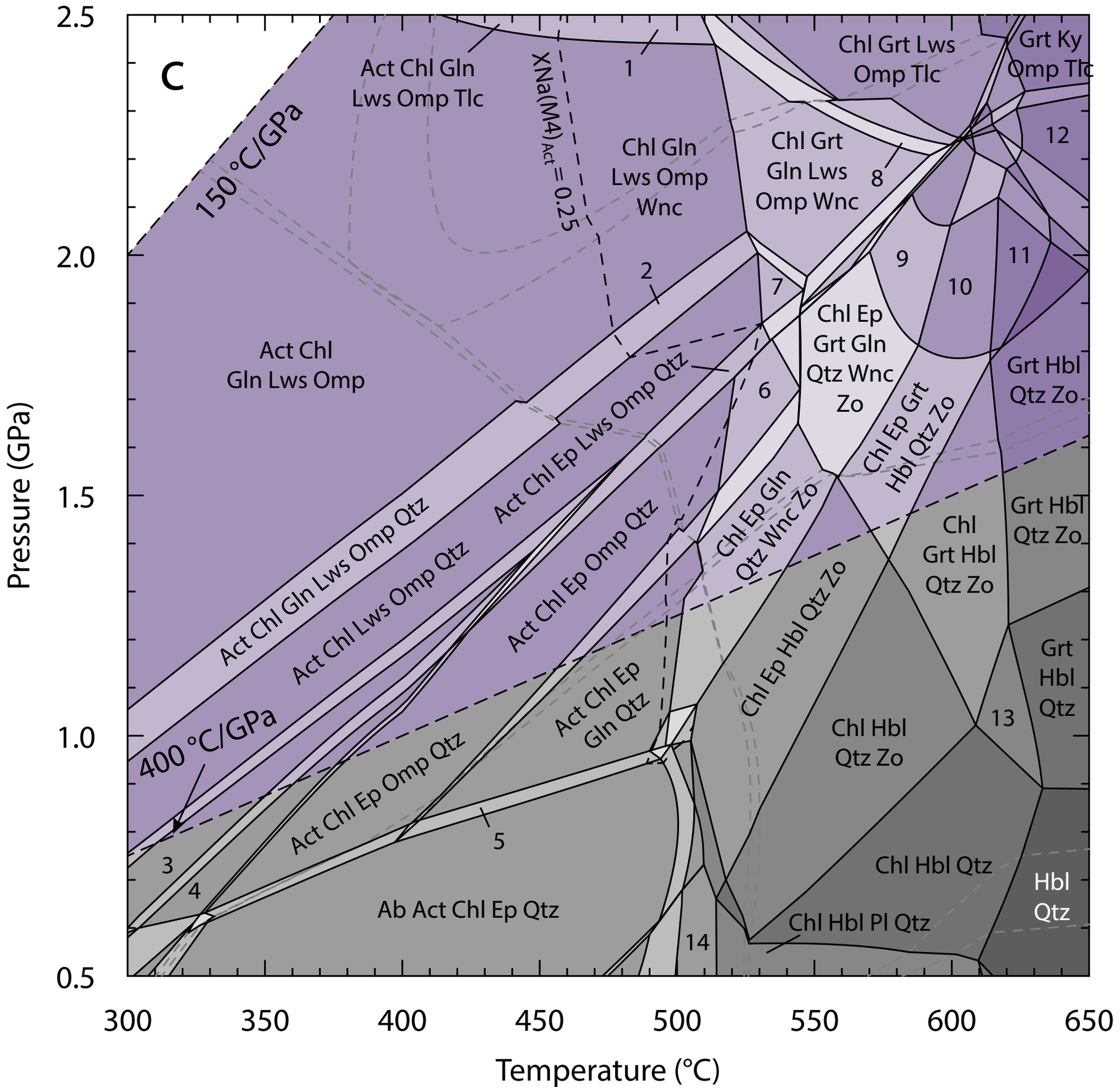
CM99 Gabbro
+ Ms/Bt, Spn/Rt/Ilm, H2O
C
150 °C/GPa
400 °C/GPa
XNa(M4)Act = 0.25
Act Chl Gln Lws Omp Tlc
Chl Gln Lws Omp Wnc
Chl Grt Lws Omp Tlc
Grt Ky Omp Tlc
Chl Grt Gln Lws Omp Wnc
Act Chl Gln Lws Omp
Act Chl Ep Lws Omp Qtz
Act Chl Lws Omp Qtz
Act Chl Gln Lws Omp Qtz
Act Chl Ep Omp Qtz
Chl Ep Grt Gln Qtz Wnc Zo
Chl Ep Grt Hbl Qtz Zo
Grt Hbl Qtz Zo
Chl Grt Hbl Qtz Zo
Chl Ep Gln Qtz Wnc Zo
Chl Ep Hbl Qtz Zo
Act Chl Ep Gln Qtz
Act Chl Ep Omp Qtz
Grt Hbl Qtz
Chl Hbl Qtz Zo
Chl Hbl Qtz
Hbl Qtz
Chl Hbl Pl Qtz
Ab Act Chl Ep Qtz
1
2
3
4
5
6
7
8
9
10
11
12
13
14
Pressure (GPa)
Temperature (°C)
2.5
2.0
1.5
1.0
0.5
300
350
400
450
500
550
600
650

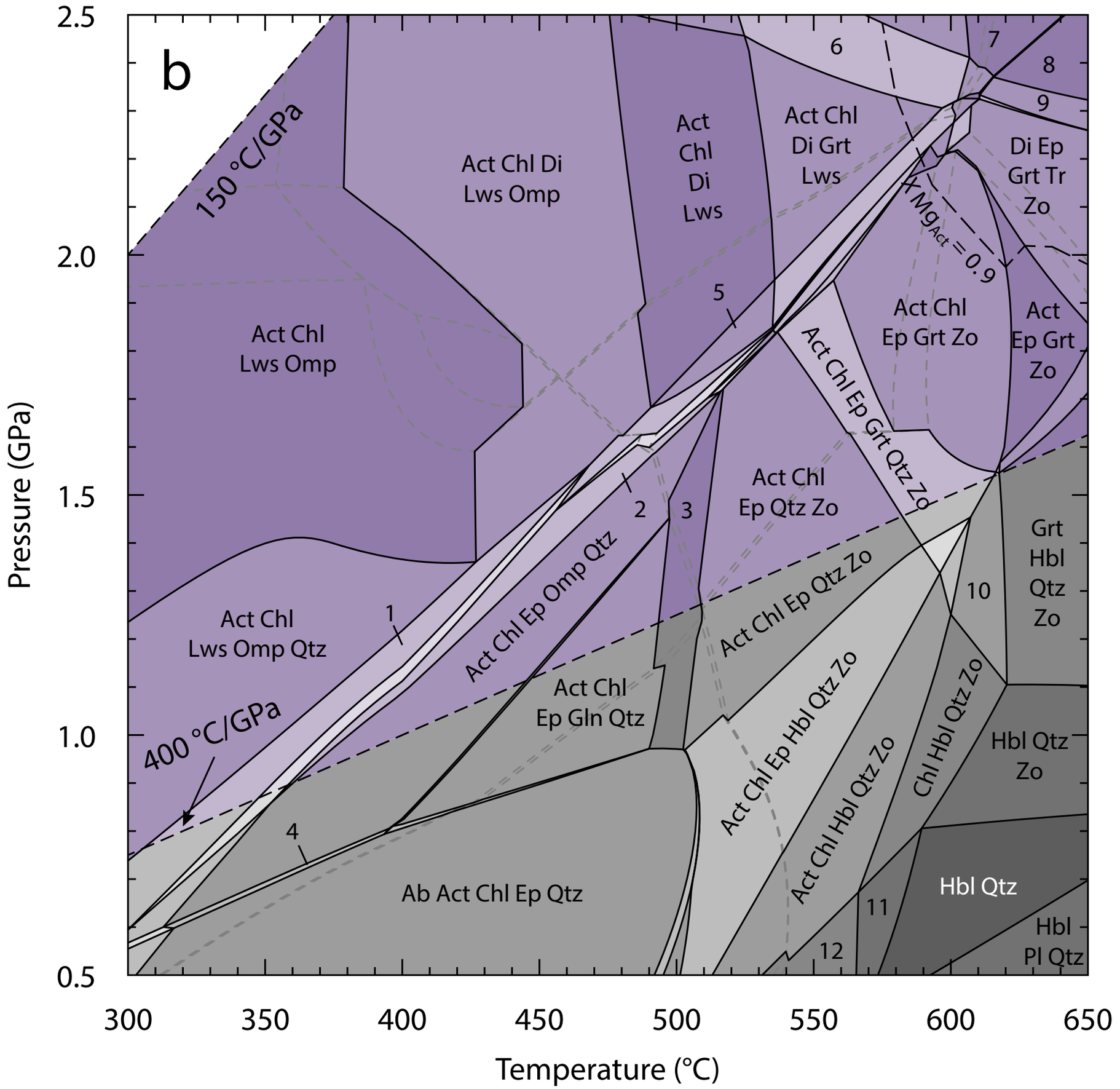
HF82 Olivine-bearing basalt
+ Ms/Bt, Spn/Rt/Ilm, H2O
b
150 °C/GPa
400 °C/GPa
Act Chl Di Lws Omp
Act Chl Lws Omp
Act Chl Lws Omp Qtz
Act Chl Di Lws
Act Chl Di Grt Lws
Di Ep Grt Tr Zo
Act Chl Ep Grt Zo
Act Ep Grt Zo
Act Chl Ep Grt Qtz Zo
Act Chl Ep Qtz Zo
Act Chl Ep Omp Qtz
Act Chl Ep Gln Qtz
Grt Hbl Qtz Zo
Act Chl Ep Hbl Qtz Zo
Act Chl Hbl Qtz Zo
Chl Hbl Qtz Zo
Hbl Qtz Zo
Ab Act Chl Ep Qtz
Hbl Qtz
Hbl Pl Qtz
XMgAct = 0.9
1
2
3
4
5
6
7
8
9
10
11
12
Pressure (GPa)
Temperature (°C)
2.5
2.0
1.5
1.0
0.5
300
350
400
450
500
550
600
650

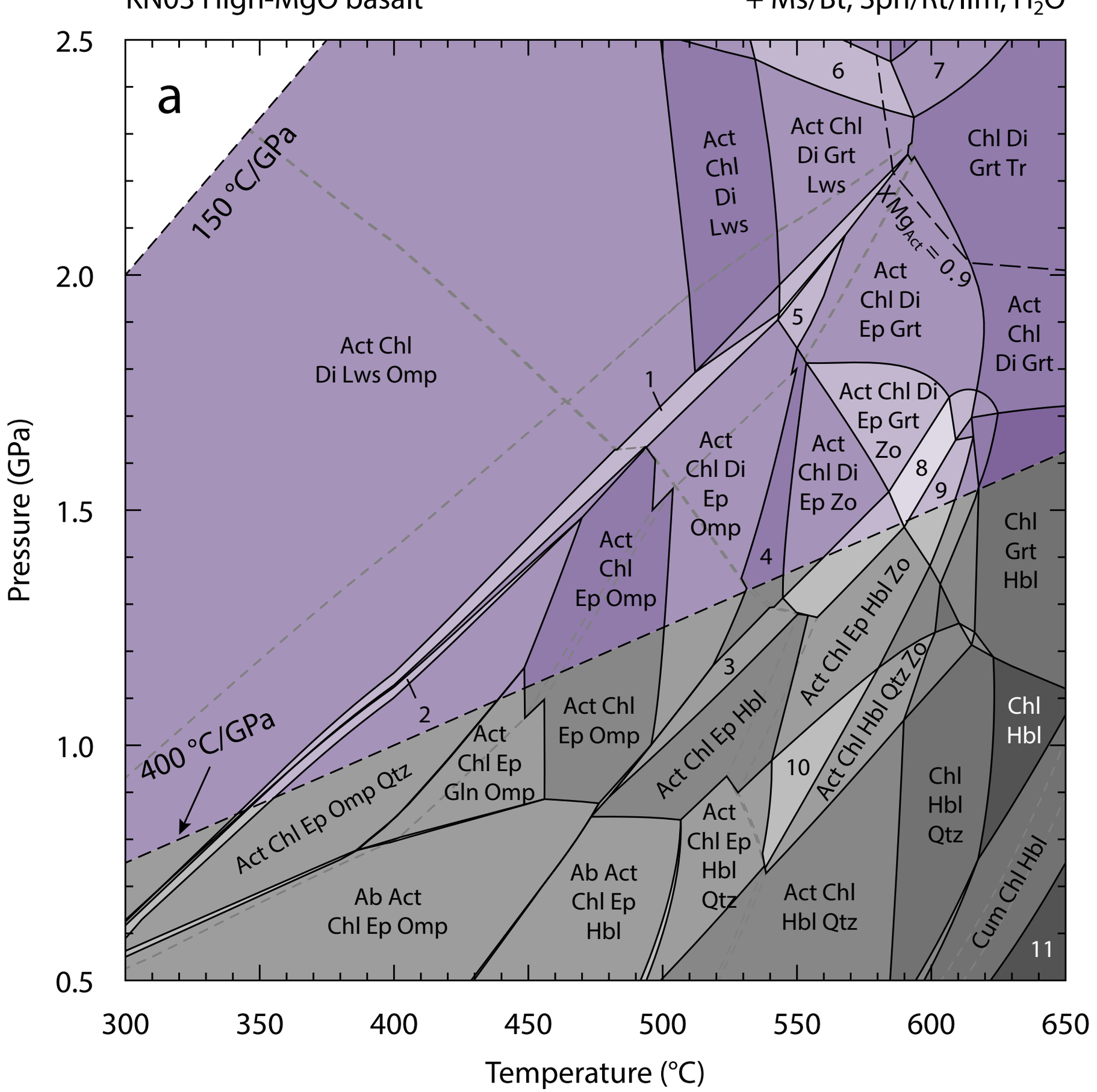
KN03 High-MgO basalt
+ Ms/Bt, Spn/Rt/Ilm, H2O
a
150 °C/GPa
400 °C/GPa
XMgAct = 0.9
Act Chl Di Lws Omp
Act Chl Ep Omp Qtz
Ab Act Chl Ep Omp
Act Chl Ep Gln Omp
Act Chl Ep Omp
Ab Act Chl Ep Hbl
Act Chl Di Ep Omp
Act Chl Ep Hbl
Act Chl Di Ep Zo
Act Chl Ep Hbl Qtz
Act Chl Hbl Qtz
Act Chl Di Ep Grt Zo
Act Chl Ep Hbl Zo
Act Chl Hbl Qtz Zo
Act Chl Di Ep Grt
Act Chl Di Grt
Act Chl Di Lws
Act Chl Di Grt Lws
Chl Di Grt Tr
Chl Grt Hbl
Chl Hbl Qtz
Chl Hbl
Cum Chl Hbl
1
2
3
4
5
6
7
8
9
10
11
Pressure (GPa)
Temperature (°C)
0.5
1.0
1.5
2.0
2.5
300
350
400
450
500
550
600
650

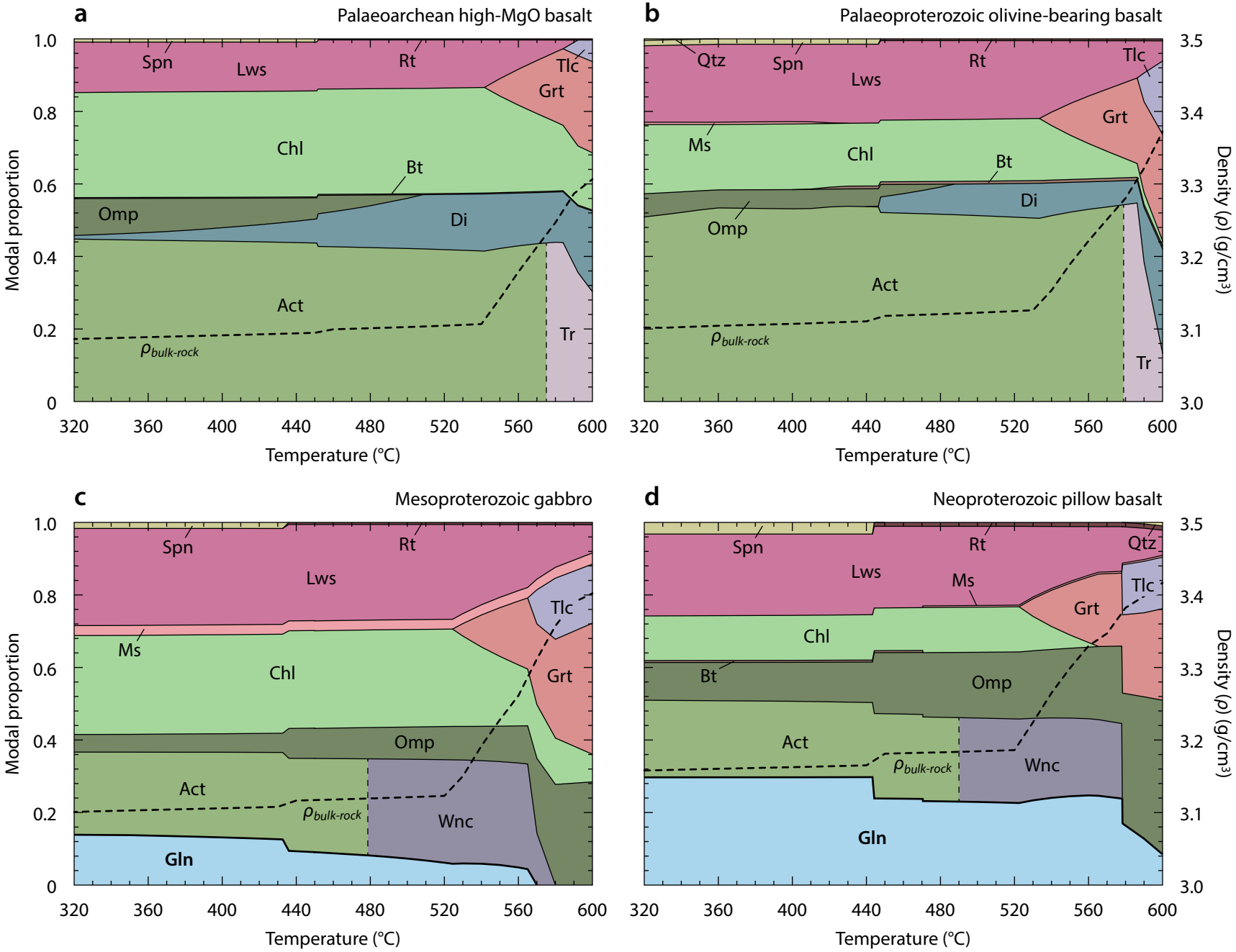
a
Palaeoarchean high-MgO basalt
b
Palaeoproterozoic olivine-bearing basalt
c
Mesoproterozoic gabbro
d
Neoproterozoic pillow basalt
Modal proportion
Density (ρ) (g/cm³)
Temperature (°C)
Spn
Lws
Rt
Tlc
Grt
Chl
Bt
Omp
Di
Act
Tr
Qtz
Ms
Wnc
Gln
ρbulk-rock

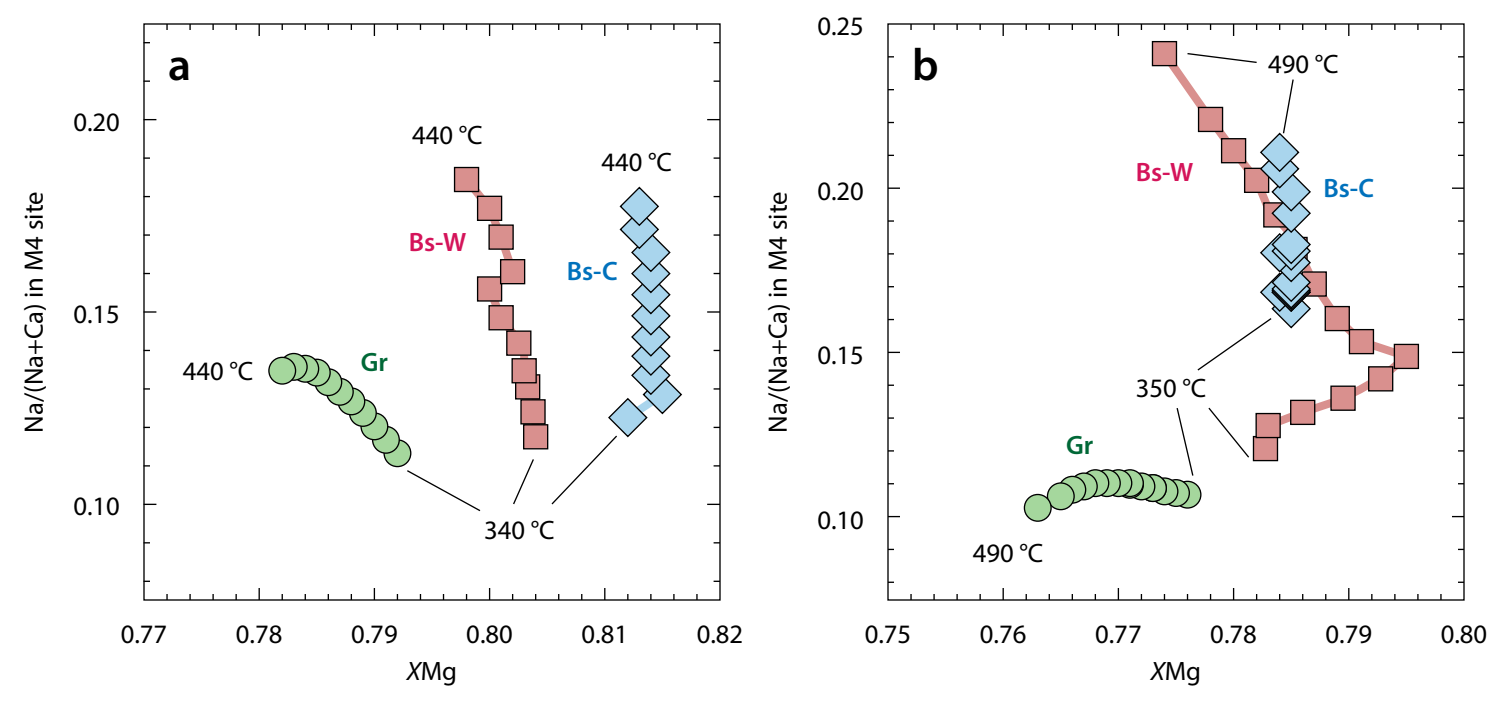
a
b
Na/(Na+Ca) in M4 site
XMg
Gr
Bs-W
Bs-C
440 °C
340 °C
490 °C
350 °C
0.10
0.15
0.20
0.25
0.75
0.76
0.77
0.78
0.79
0.80
0.81
0.82